



UvA-DARE (Digital Academic Repository)

The Fundamental Plane of Black Hole Accretion and Its Use as a Black Hole-Mass Estimator

Gültekin, K.; King, A.L.; Cackett, E.M.; Nyland, K.; Miller, J.M.; Di Matteo, T.; Markoff, S.; Rupen, M.P.

DOI

[10.3847/1538-4357/aaf6b9](https://doi.org/10.3847/1538-4357/aaf6b9)

Publication date

2019

Document Version

Final published version

Published in

Astrophysical Journal

[Link to publication](#)

Citation for published version (APA):

Gültekin, K., King, A. L., Cackett, E. M., Nyland, K., Miller, J. M., Di Matteo, T., Markoff, S., & Rupen, M. P. (2019). The Fundamental Plane of Black Hole Accretion and Its Use as a Black Hole-Mass Estimator. *Astrophysical Journal*, 871(1), [80]. <https://doi.org/10.3847/1538-4357/aaf6b9>

General rights

It is not permitted to download or to forward/distribute the text or part of it without the consent of the author(s) and/or copyright holder(s), other than for strictly personal, individual use, unless the work is under an open content license (like Creative Commons).

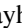


Disclaimer/Complaints regulations

If you believe that digital publication of certain material infringes any of your rights or (privacy) interests, please let the Library know, stating your reasons. In case of a legitimate complaint, the Library will make the material inaccessible and/or remove it from the website. Please Ask the Library: <https://uba.uva.nl/en/contact>, or a letter to: Library of the University of Amsterdam, Secretariat, Singel 425, 1012 WP Amsterdam, The Netherlands. You will be contacted as soon as possible.

UvA-DARE is a service provided by the library of the University of Amsterdam (<https://dare.uva.nl>)



The Fundamental Plane of Black Hole Accretion and Its Use as a Black Hole-Mass Estimator

Kayhan Gültekin¹ , Ashley L. King², Edward M. Cackett³ , Kristina Nyland⁴, Jon M. Miller¹, Tiziana Di Matteo⁵, Sera Markoff^{6,7} , and Michael P. Rupen⁸

¹ Department of Astronomy, University of Michigan, 500 Church Street, Ann Arbor, MI 48109, USA; kayhan@umich.edu

² KIPAC, Stanford University, 452 Lomita Mall, Stanford, CA 94305 USA

³ Department of Physics and Astronomy, Wayne State University, 666 W. Hancock Street, Detroit, MI 48201, USA

⁴ National Radio Astronomy Observatory, Charlottesville, VA 22903, USA

⁵ McWilliams Center for Cosmology, Physics Department, Carnegie Mellon University, Pittsburgh, PA 15213, USA

⁶ Anton Pannekoek Institute for Astronomy, University of Amsterdam, Science Park 904, 1098 XH Amsterdam, The Netherlands

⁷ Gravitation Astroparticle Physics Amsterdam (GRAPPA) Institute, University of Amsterdam, Science Park 904, 1098 XH Amsterdam, The Netherlands

⁸ National Research Council of Canada, Herzberg Astronomy and Astrophysics, Dominion Radio Astrophysical Observatory, P.O. Box 248, Penticton, BC V2A 6J9, Canada

Received 2017 November 20; revised 2018 November 26; accepted 2018 November 27; published 2019 January 23

Abstract

We present an analysis of the fundamental plane of black hole accretion, an empirical correlation of the mass of a black hole (M), its 5 GHz radio continuum luminosity (νL_ν), and its 2–10 keV X-ray power-law continuum luminosity (L_X). We compile a sample of black holes with primary, direct black hole-mass measurements that also have sensitive, high-spatial-resolution radio and X-ray data. Taking into account a number of systematic sources of uncertainty and their correlations with the measurements, we use Markov chain Monte Carlo methods to fit a mass-predictor function of the form $\log(M/10^8 M_\odot) = \mu_0 + \xi_{\mu R} \log(L_R/10^{38} \text{ erg s}^{-1}) + \xi_{\mu X} \log(L_X/10^{40} \text{ erg s}^{-1})$. Our best-fit results are $\mu_0 = 0.55 \pm 0.22$, $\xi_{\mu R} = 1.09 \pm 0.10$, and $\xi_{\mu X} = -0.59^{+0.16}_{-0.15}$ with the natural logarithm of the Gaussian intrinsic scatter in the log-mass direction $\ln \epsilon_\mu = -0.04^{+0.14}_{-0.13}$. This result is a significant improvement over our earlier mass scaling result because of the increase in active galactic nuclei sample size (from 18 to 30), improvement in our X-ray binary sample selection, better identification of Seyferts, and improvements in our analysis that takes into account systematic uncertainties and correlated uncertainties. Because of these significant improvements, we are able to consider potential influences on our sample by including all sources with compact radio and X-ray emission but ultimately conclude that the fundamental plane can empirically describe all such sources. We end with advice for how to use this as a tool for estimating black hole masses.

Key words: accretion, accretion disks – black hole physics – galaxies: active – galaxies: jets – galaxies: nuclei

Supporting material: Interactive Figure

1. Introduction

Accretion and outflows, including jets, are seen in many astrophysical objects and are thought to have an intimate, physical connection to each other. Among all of the objects seen to have accretion and outflows (e.g., protostars, white dwarfs, and neutron stars), black holes have the greatest range in mass so correlations with mass can be tested.

An important observational connection related to accretion–jet phenomena was first noted by Hannikainen et al. (1998) in a power-law relation between the radio and X-ray fluxes of black hole candidate GX 339-4 at various levels of low/hard states. Compiling many such black hole X-ray binaries (XRBs), Gallo et al. (2003) found that many black hole XRBs followed a similar trend such that the radio luminosity (L_R) of a low/hard state XRB scales with the X-ray luminosity (L_X) as $L_R \sim L_X^{0.7}$. This same observational trend was examined in active galactic nuclei (AGNs) but found to depend on the mass of the black hole (M) as well (Merloni et al. 2003; Falcke et al. 2004). Because the masses of XRB black holes are all within a factor of a few of each other, such a scaling is only apparent when it is examined across several orders of magnitude. This M – L_R – L_X relation is often called the fundamental plane of black hole activity because it occupies a two-dimensional manifold in the three-dimensional space.

The empirical relation of the fundamental plane has been used to generate insights about the physics of accretion onto black holes. Merloni et al. (2003) interpreted the fundamental plane as the result of scale invariant disk–jet coupling relating jet power probed by radio and mass accretion rate probed by X-rays. This interpretation was based on work by Markoff et al. (2003), which was later generalized by Heinz & Sunyaev (2003) and then extended by Heinz (2004) to include the effects of synchrotron cooling. Falcke et al. (2004) interpreted the fundamental plane as arising from sub-Eddington jet-dominated systems in which the emission arises from the jet as optically thick radio synchrotron and optically thin X-ray synchrotron. For a description of the similarities and differences among these interpretations, see the discussion by Plotkin et al. (2012). An additional interpretation provided by Yuan & Cui (2005) argues for a critical X-ray Eddington ratio below which the fundamental plane switches from accretion-flow-dominated X-ray to jet-dominated emission.

After the initial discovery studies, the empirical relation was pushed to a wider variety of accreting black hole sources. Wang et al. (2006) considered the fundamental plane in radio-active Type 1 AGNs and found only a weak dependence on mass, opening the possibility that AGNs with $L_X/L_{\text{Edd}} > 10^{-3}$ follow a completely different relation. Their work was followed up by Li et al. (2008) with a larger sample and showed a significant

Table 1
New 8.4 GHz VLA Data

Galaxy	SB ID	MJD	Flux Cal.	Gain Cal.	S_{peak} mJy	S_{ν} mJy	rms mJy	Size " × "	PA °
NGC 1300	3035251	55747	3C138	J0340-2119	0.530	0.582 ± 0.042	0.018	0.37×0.23	168
NGC 2748	4463759	55744	3C147	J0930+7420	0.134	0.197 ± 0.051	0.019	0.36×0.25	26
NGC 2778	4463837	55745	3C147	J0916+3854	0.109	0.115 ± 0.039	0.019	0.26×0.20	55
NGC 3384	4463932	55735	3C288	J1044+0655	...	<0.047	0.016
NGC 4291	4464121	55724	3C295	J1243+7442	...	<0.143	0.048
NGC 4459	4464418	55723	3C286	J1230+1223	0.496	0.428 ± 0.034	0.017	0.23×0.20	38
NGC 4486A	4464517	55737	3C286	J1230+1223	...	<0.273	0.020
NGC 4596	4464593	55737	3C286	J1230+1223	0.105	0.102 ± 0.046	0.023	0.30×0.22	32
NGC 4742	4464671	55735	3C286	J1256-0547	...	<0.127	0.015
NGC 5077	4464763	55742	3C286	J1337-1257	185.4	193.1 ± 5.8	0.222	0.30×0.23	4
NGC 5576	4464855	55740	3C295	J1405+0415	...	<0.202	0.067
NGC 7457	4466045	55743	3C48	J2255+4202	...	<0.057	0.019

Note. This table lists results from our new 8.4 GHz VLA observing campaign. The columns list host galaxy name, VLA scheduling block identification number, MJD of the observation, flux calibrator, gain calibrator, and 8.4 GHz flux density. Upper limits are listed at their 3σ value.

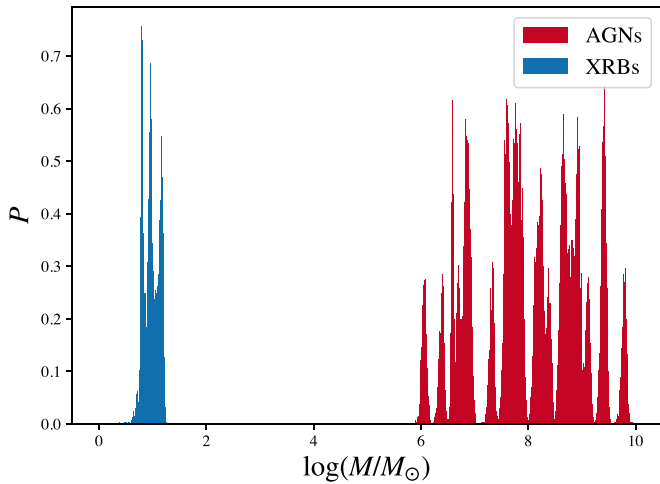


Figure 1. Probability density of black hole masses for the entire sample. We plot multiple realizations of our sample from the masses with uncertainties and their dependence on distance for the AGN sample. Thus, the distribution of the probability density of an individual black hole’s mass combines the statistical measurement uncertainties of both the mass and the distance. We do not include distance uncertainty in the XRB mass probability density because it generally does not affect it. The range of masses included in our sample is illustrated in this figure.

difference in fundamental plane fits for radio-quiet and radio-loud samples of Type 1 AGN. Panessa et al. (2007) found a significant correlation between L_R and L_X in a sample of Seyfert galaxies and low-luminosity radio galaxies. Although there were concerns that the fundamental plane was a manifestation of distance creating the illusion of a luminosity–luminosity relation, partial correlation analyses showed that the fundamental plane relations were not driven by distance (Merloni et al. 2003, 2006; Wang et al. 2006).

Work from the last five years has used even larger samples to further promote the understanding of the underlying physics of the fundamental plane. Plotkin et al. (2012) used a carefully selected sample of BL Lac objects to supplement a selection of low-luminosity AGNs and XRBs, arguing that when the radio spectrum is flat/inverted, the X-ray emission comes from jet synchrotron. Further examination of the L_R – L_X relation in XRBs has uncovered multiple tracks rather than a universal relation (Gallo et al. 2012). The existence of multiple tracks raises the

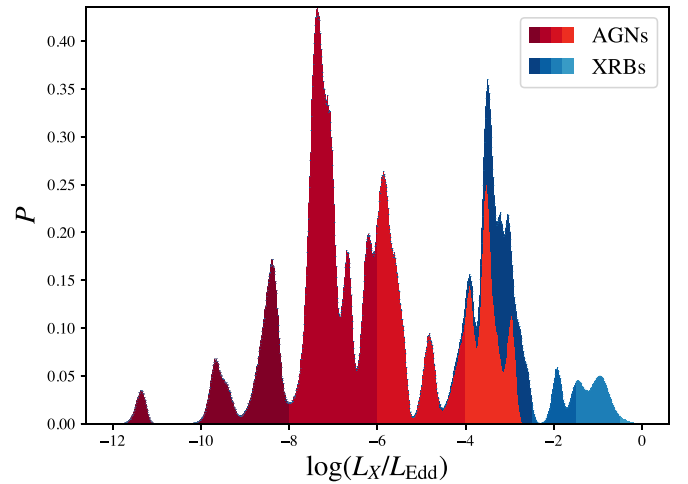


Figure 2. Probability density of logarithmic 2–10 keV X-ray Eddington fraction. We plot multiple realizations of our sample using statistical uncertainties of X-ray flux, distance to source, and black hole mass. For AGN sources, we take into account the correlation between distance in the luminosity calculation and distance in the mass estimate. The multiple observations of individual XRBs are incorporated by weighting each as $1/N$, where N is the number of observations of a given XRB. The probability density curves are colored according to mass category (red for AGNs and blue for XRBs) and the shade is given by the value of $\log(L_X/L_{\text{Edd}})$. AGNs are grouped into the following discrete bins: $(-\infty, -8)$, $[-8, -6)$, $[-6, -4)$, and $[-4, +\infty)$. XRBs are grouped into the following discrete bins: $(-\infty, -2.5)$, $[-2.5, -1.5)$, $[-1.5, -0.5)$, and $[-0.5, +\infty)$. We use this color scheme in figures throughout this paper. Note that the probability density plotted is the total probability density of all sources so that at, e.g., $\log(L_X/L_{\text{Edd}}) = -4$, the probability density is dominated by AGNs with a small contribution coming from XRBs. The nearly 10 orders of magnitude in X-ray Eddington fraction covered by our sample is illustrated in this figure.

possibility of more complex physical underpinnings of the fundamental plane and led to work by Dong et al. (2014) to observe that radiatively efficient XRBs and AGNs follow their own, separate fundamental plane. Fan & Bai (2016) demonstrated that the fundamental plane for compact steep-spectrum radio sources was best explained by a hot corona origin for X-ray emission. In the faintest objects, with $L_X/L_{\text{Edd}} < 10^{-6}$, the fundamental plane observed by Xie & Yuan (2017) argue for X-ray emission coming from hot thermal gas in the accretion flow as predicted by Yuan & Cui (2005), though this idea was ruled out by Plotkin et al. (2013).

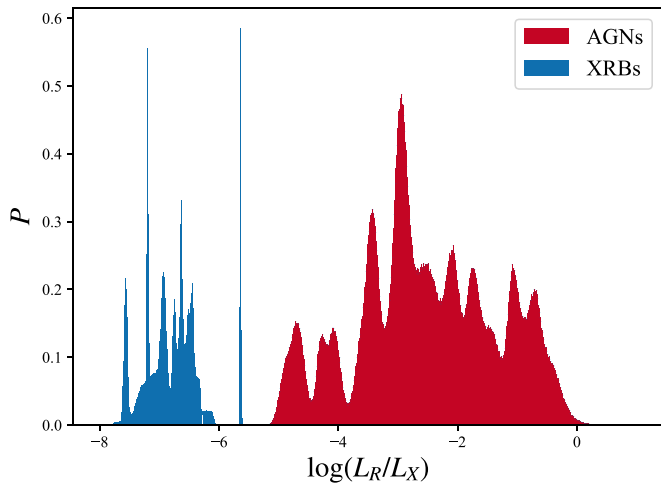


Figure 3. Probability density of the logarithmic ratio of radio to X-ray luminosity. We plot multiple realizations of our sample using statistical uncertainties of radio flux and X-ray flux. As in the rest of this paper, radio “luminosity” is defined as $L_R \equiv \nu L_\nu$, for $\nu = 5$ GHz, whereas the X-ray luminosity is a true 2–10 keV bandpass luminosity. The uncertainty in the radio luminosity also incorporates our estimate of systematic uncertainty in converting from other frequencies to 5 GHz. The nearly 8 orders of magnitude probed by our sample is illustrated in this figure as is the larger fractional uncertainties in the AGNs.

In addition to the insights it may provide regarding accretion physics, the fundamental plane is also interesting because it relates two relatively simple electromagnetic observations, L_R and L_X , to a notoriously difficult one, M . A black hole’s mass is of paramount interest, as mass and spin are the only two parameters intrinsic to an astrophysical black hole. It also sets the scale for accretion properties for such things as the Eddington luminosity, L_{Edd} . The Eddington fraction $f_{\text{Edd}} \equiv L_{\text{bol}}/L_{\text{Edd}}$, in fact, may be the most important parameter of an AGN (Boroson & Green 1992; Sulentic et al. 2000; Boroson 2002; Shen & Ho 2014). Black hole mass also sets relative size scales, including the Schwarzschild radius, the innermost stable circular orbit radius, and the the black hole shadow size (Doeleman et al. 2008).

Although black hole mass estimation methods exist at varying levels of resource intensiveness (e.g., stellar dynamics, Gültekin et al. 2009b; reverberation mapping, Peterson 2014; and host scaling relations, Gültekin et al. 2009c), the ability to use radio and X-ray observations to estimate black hole mass would be a useful additional method in cases where other methods do not work well. It may be useful, for example, for (i) distinguishing between XRBs, accreting intermediate-mass black holes (IMBHs), and AGNs; (ii) determining the mass of a black hole in a Type 2 AGN in a host galaxy with disturbed morphology making host-galaxy scaling relations unusable; or (iii) investigating the evolution of host-galaxy scaling relations with redshift.

The fundamental plane has been used to estimate black hole masses in a number of cases where other methods were not viable. For instance, this plane was used to claim the presence of a $10^6 M_\odot$ black hole in the dwarf starburst galaxy Henize 2–10, which had no obvious spheroidal component from which one could use host scaling relations (Reines et al. 2011). Miller & Gültekin (2011) used the fundamental plane to estimate the mass of the black hole in the tidal disruption event Swift J164449.3+573451. The latter case assumes that the fundamental plane is appropriate at high—probably super-Eddington—accretion rates expected from a tidal disruption event.

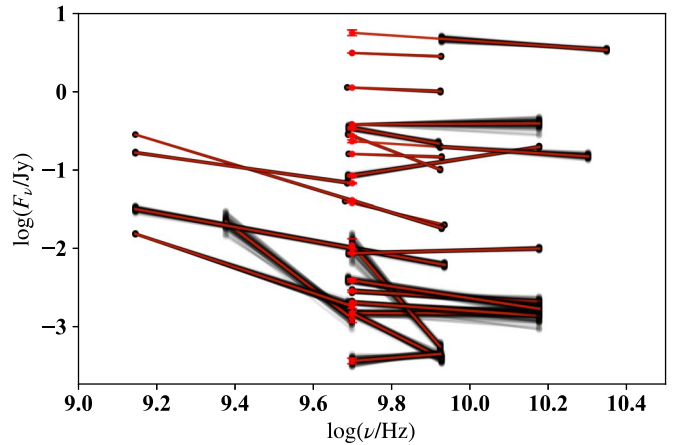


Figure 4. A summary plot of radio data for all AGN for which we have calculated radio spectral indexes (α). Each set of black lines was constructed by doing Monte Carlo simulations of the measurements of the source at each frequency assuming a Gaussian distribution with dispersion equal to their 1σ uncertainties. Because the sources are all at low redshift, the correlated uncertainties in distance do not come into effect here, and we just plot flux density. Then, we calculate α for the two values. We do this for 10^5 realizations, but we only plot a random subset of 100 of them. For using a single value of alpha for our tables, we use the median value of alpha with the 68% intervals for our 1σ uncertainties. We plot, in red, the median value and the median interpolated/extrapolated value for the 5 GHz F_ν value with 1σ error. Although we plot the medians for reference, we use the Monte Carlo realizations for each of our fit realizations. In this way, e.g., a source with $\alpha = 0.3 \pm 0.1$, will be classified and treated as a flat source for the roughly 84% of the time that $\alpha < 0.4$.

In Gültekin et al. (2009a), we looked at the fundamental plane for a sample of AGNs that have direct, primary measurements of black hole mass to eliminate this source of systematic uncertainty. We found a number of potentially interesting empirical results, but it was not clear whether these arose because of actual correlations or because of the relatively small number (18) of AGNs with direct, primary M measurements that also have suitable X-ray and radio data. In this current paper, we use new data to continue our study of the fundamental plane with black holes with direct, primary mass measurements. The use of such mass measurements enables us (i) to eliminate the systematic uncertainty of using secondary measurements and (ii) to calibrate the relation for use as a mass estimator. We use the X-ray data from Gültekin et al. (2012) as well as hitherto unpublished radio data plus archival and data from the literature to make the largest M – L_R – L_X analysis for black holes with dynamical mass measurements to date now including 30 AGN sources and 6 XRB sources. We discuss our sample selection and standards for mass, radio, and X-ray data inclusion in Section 2. In Section 3 we describe our fitting methodology and results from the fundamental plane fit to the data. We discuss our results in Section 4 and conclude with advice for how to use the fundamental plane to estimate black hole mass in Section 5. Appendices C–D contain details of the new and archival data analysis used in this paper.

2. Sample

In this section we describe our sample. Because of the differences in the two, we discuss the AGN and XRB samples separately. The data are summarized in Figures 1–3 and listed completely in Tables 1–6. We note here that there is significant improvement in the sample here over our earlier sample of Gültekin et al. (2009a). We have increased the AGN sample from 18 to 30, and inclusion in the current expanded XRB sample

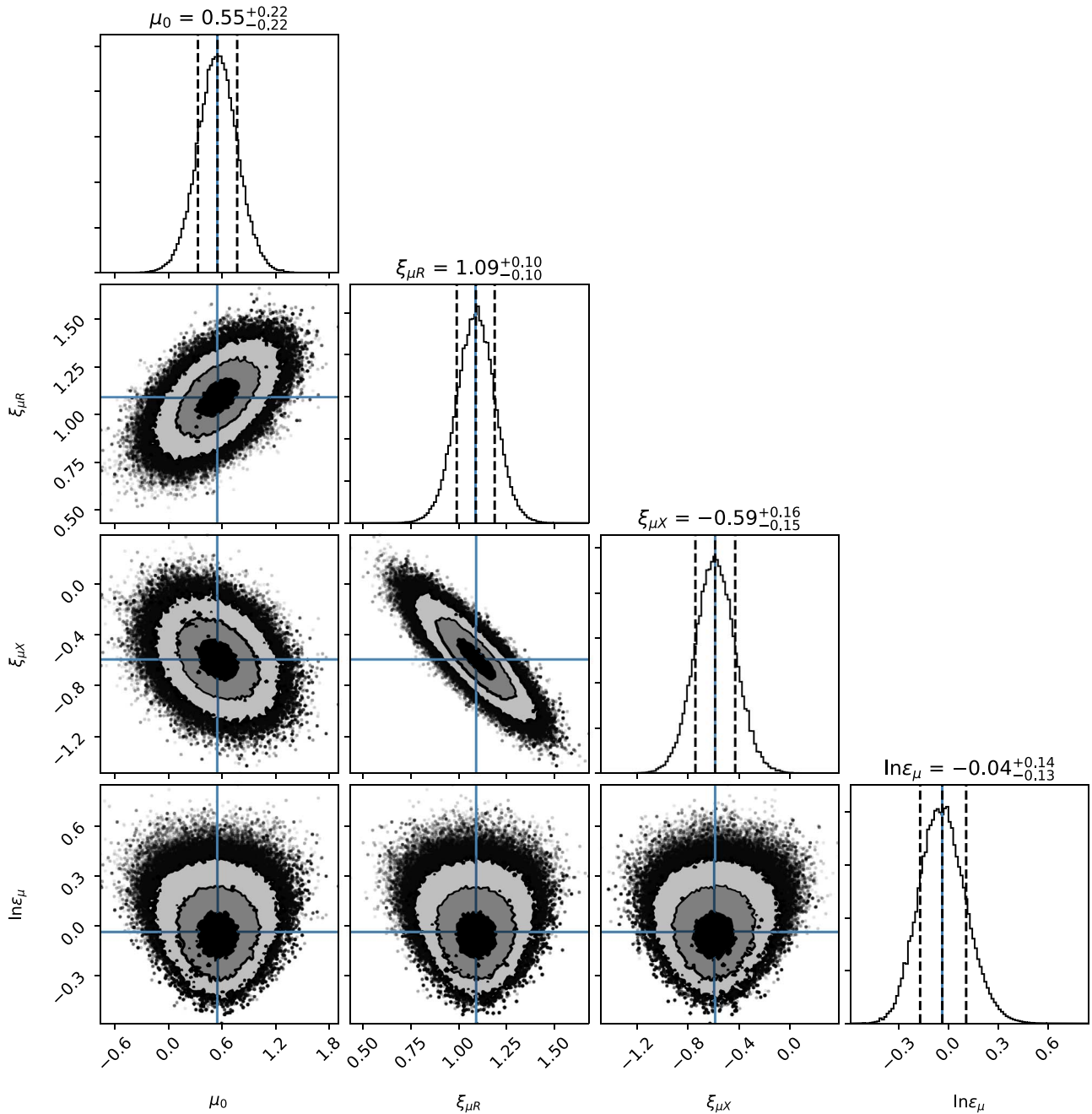


Figure 5. A Foreman-Mackey (2016) corner plot of MCMC results. Each panel in this corner plot of our MCMC results shows either the posterior probability distribution of an individual parameter in our fits (histograms) or the joint posterior probability distribution of pairs of parameters (scatter plots). The equations at the top of each column show the median and 68% interval of each parameter, $\mu_0 = 0.55 \pm 0.22$, $\xi_{\mu R} = 1.09 \pm 0.10$, $\xi_{\mu X} = -0.59^{+0.16}_{-0.15}$, and $\ln \epsilon_\mu = -0.04^{+0.14}_{-0.13}$. The posterior distributions show well-behaved, mono-modal distributions. The joint posterior distributions show some covariance between $\xi_{\mu R}$ and $\xi_{\mu X}$ as well as between μ_0 and either of $\xi_{\mu R}$ and $\xi_{\mu X}$. The asymmetry in the joint posterior distributions that include $\ln \epsilon_\mu$ is typical when using a logarithmic intrinsic scatter term. For comparison, the corresponding fits from Gültekin et al. (2009a) are $\mu_0 = 0.19 \pm 0.19$, $\xi_{\mu R} = 0.48 \pm 0.16$, $\xi_{\mu X} = -0.24 \pm 0.15$, and $\ln \epsilon_\mu = -0.26$.

required stricter mass and distance determinations changing the number from 3 to 6. We also have improved AGN classification (Section 2.1.4).

2.1. AGNs

The ideal data set of AGNs will have a large number of sources with multiple, independent measurements of mass, strictly simultaneous measurements of the X-ray and radio fluxes at the highest possible spatial resolution in multiple bands. Such ideal data do not exist, and thus we have made a number of

compromises in terms of simultaneity and multiple bands. To mitigate the impact of these compromises, we have implemented a number of measures, which we describe below. Overall, these measures help ensure that our final results are robust and meaningful.

2.1.1. Mass Estimates

We require our AGN sources to have primary, direct dynamical mass measurements. This requirement implies that all black hole-mass measurements were done using stellar

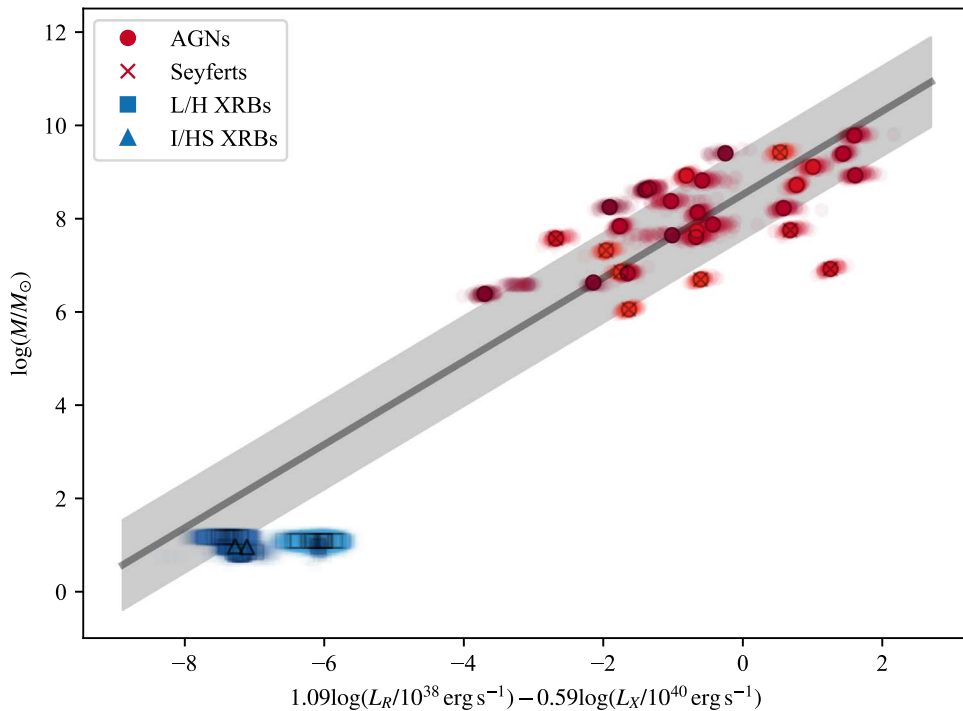


Figure 6. Edge-on view of the fundamental plane with mass as dependent variable. Here we plot all data realized N times to show the correlated uncertainties. Colors are as in Figure 2, and symbols indicate whether the source is an AGN (red circles), a Seyfert AGN (red circle with cross), an XRB in a low/hard state (blue squares), or an XRB in an intermediate or high/soft state (blue triangles). Each source is sampled from its measurement uncertainties as is done in the fitting procedure and is plotted with a partially transparent symbol plus a dark outline symbol on top at the nominal values. We plot the best-fit relation as a dark gray line with a light gray shaded region to indicate the 1σ region of the Gaussian intrinsic scatter, which has magnitude of 1 dex. This figure summarizes the results of the fits as well as indicates the fidelity with which one can use the fundamental plane to estimate black hole mass.

dynamical (e.g., Gültekin et al. 2009b), gas dynamical (e.g., Walsh et al. 2010), or megamaser techniques (e.g., Kuo et al. 2011). Because reverberation mapping techniques (Blandford & McKee 1982) mostly rely on normalizing the mass estimates to the primary measurements and thus are not independent, we do not include them. Requiring that mass measurements be independent is essential for using the fundamental plane as a mass estimator.

Our sample of AGNs begins with the compilation of primary, direct dynamical mass measurements in Kormendy & Ho (2013). We supplement their compilation with upper limits compiled by Gültekin et al. (2009c). We also adopt the distances determined by Kormendy & Ho (2013), unless they are unavailable, in which case we use the value determined by Gültekin et al. (2009c). We note that NGC 1399 has two stellar dynamical mass measurements (Houghton et al. 2006; Gebhardt et al. 2007) that are independently reliable but inconsistent with each other. Gültekin et al. (2009c) and Kormendy & Ho (2013) took both results into consideration, but given the larger number of tests done by the code used in the Gebhardt et al. (2007) result, we use only their mass value. All AGN sources are listed by host galaxy name in Table 5, including black hole masses (M) along with the references for the measurement.

2.1.2. Radio Data

The ideal radio data for this project requires good spatial resolution to isolate the nuclear core flux with good point-source sensitivity to reach as deep as possible to avoid having only an upper limit. This effectively requires sensitive radio interferometry, ideally with NSF’s Karl G. Jansky Very Large

Array (VLA), which has a resolution of about $0''.4$ at 5 GHz, corresponding to 40 pc at a distance of 20 Mpc. Whenever possible, we have used VLA data either from the modern epoch or from earlier epochs, but we have also used data from other radio interferometers and even single-dish data for a few sources. We use the 5 GHz band as the frequency of reference to be compatible with other fundamental plane studies, but we do not require that the observations be taken at this frequency. We do not make such a requirement because (i) the radio spectra near 5 GHz are almost always power-law spectra that can be relatively easily translated to 5 GHz, (ii) at higher frequencies the spatial resolution is superior, allowing better isolation of nuclear core flux from contaminants, and (iii) limiting ourselves to 5 GHz would severely limit the amount of archival and literature data at our disposal. We discuss how we translate to 5 GHz in further detail in Section 3.1.3. The data in this paper come from (i) our previous analysis of archival data (Gültekin et al. 2009a), (ii) results published in the literature, (iii) our analysis of previously unpublished data obtained for this project (Appendix A), and (iv) our analysis of archival data (Appendix B).

2.1.3. X-Ray Data

The ideal X-ray data for our project requires good spatial resolution to isolate the nuclear flux as best as possible and good sensitivity to reach to low Eddington fractions. This effectively requires moderate to long exposures with the *Chandra X-ray Observatory* (*Chandra*), which has a 90% encircled energy radius of about $0''.8$ at 1.5 keV. Therefore, we only use *Chandra* observations of our selected AGN. As with other fundamental plane studies, we use the 2–10 keV flux

Table 2
Archival VLA Data

Galaxy	Array	MJD	ν /GHz	S_{ν} /mJy
IC 4296	VLA A	52381	8.46	247.7 ± 1.7
IC 1459	VLA A	52301	4.86	1126 ± 56
NGC 0224	VLA B	52485	8.40	<0.06
NGC 1068	VLA A	51429	8.46	364 ± 23
NGC 1399	VLA A	45608	4.88	5.7 ± 0.7
NGC 1550	VLA B	51033	8.48	<0.5
NGC 2787	VLA A	51899	8.46	13.5 ± 0.9
NGC 3031	VLA A	51899	8.46	153 ± 7.6
NGC 3245	VLA A	53259	8.46	1.7 ± 0.15
NGC 3351	VLA AB	48596	4.88	<13.5
NGC 3393	VLA AB	52907	22.44	<13.2
NGC 3842	VLA A	47498	4.83	<1.1
NGC 4258	VLA A	51899	8.46	2.88 ± 0.18
NGC 4477	VLA A	56279	5.50	0.12 ± 0.02
NGC 4486	VLA A	52793	8.44	2803 ± 141
NGC 4594	VLA A	53280	8.46	59.9 ± 3.7
NGC 4649	VLA A	50888	8.46	18.5 ± 1.0
NGC 4889	VLA AB	47593	4.86	<2.7
NGC 5128	VLA A	53353	8.46	4700 ± 250
NGC 7052	VLA A	50907	8.46	47.5 ± 2.4
NGC 7619	VLA A	46049	4.89	1.92 ± 0.12
UGC 3789	VLA A	54791	8.44	<5.4

Note. This table lists results from our VLA archival analysis. The columns list host galaxy name, array configuration, MJD of the observation, frequency of the observation, and flux density. Upper limits are listed at their 3σ value.

arising from a power-law spectral component of the continuum emission from the AGN. If present, we exclude any emission lines in the bandpass. By using the 2–10 keV bandpass, we avoid most problems arising from inferring intrinsic flux in the presence of absorption. The AGN X-ray data in this paper come from (i) our previous analysis of archival data (Gültekin et al. 2009a), (ii) our previous analysis of *Chandra* data obtained for this project (Gültekin et al. 2012), and (iii) an analysis of archival X-ray data presented in this paper in Appendix C.

2.1.4. AGN Classification

One of the goals of this project is to determine whether or not the X-ray and radio emission by Seyferts are explained by the same fundamental plane as low-luminosity AGNs (LLAGNs) and low-hard XRBs. Therefore we include data from both Seyferts and LLAGNs. We return to this topic in Section 4.4 in which we discuss how we identify Seyferts based on classification by Ho et al. (1997) and inspection of the X-ray spectrum.

2.2. XRBs

We choose XRBs with well measured black hole masses and distances for which there are strictly or nearly simultaneous radio and X-ray data. It is obvious that an analysis of a relation among mass, radio luminosity, and X-ray luminosity requires mass measurements to be accurate and to have reliable measurement uncertainties. The distances to the XRBs are essential for turning the measured radio and X-ray fluxes into luminosities. The need for simultaneity arises from the variability of XRBs on timescales as short as hours. These selection requirements leave us with six black hole XRBs,

which we list in Table 4. While most of the XRB data come from accreting systems in the low/hard state, we also include a few data from XRBs that are in an intermediate, high/soft state, or very high state. Although XRBs are generally considered to have had their jets quenched when leaving the low/hard state and thus should not go on the fundamental plane, we include them even if they are in a state other than low/hard so long as they have measurable radio flux densities. We return to this topic in Section 4. The XRB data come from a combination of literature mass, radio, and X-ray measurements with archival analysis of *Ross X-ray Timing Explorer (RXTE)* data for a few sources (Appendix D). The requirement for *Chandra* X-ray data for AGNs does not extend to XRBs as they do not suffer from the same level of contamination issues.

We note that the sample here differs from Gültekin et al. (2009a) in that we have increased our sample size from 3 XRBs to 6, keeping GRS 1915+105 and Cygnus X-1, dropping V404 Cyg because of questions raised about its nature during its outburst in 2015 (Barthelmy et al. 2015; King et al. 2015; Kuulkers et al. 2015), and adding XTE J1118+480, 4U 1543-47, XTE J1550-564, and GRO J1655-40. The Gültekin et al. (2009a) sample had a total of 5 observations (2 of GRS 1915+105, 2 of Cygnus X-1, and 1 of V404 Cyg), whereas in this work we have 69 total observations split as shown in Table 6 with at least two observations of each.

3. Fitting the Fundamental Plane

The primary analysis of this paper is to fit the fundamental plane to the data gathered in Section 2 with special consideration of uncertainties. In this section, we first describe our Markov chain Monte Carlo (MCMC) fitting methodology and our treatment of statistical and systematic uncertainties. Then, we present the results of the fits. The fitting and handling of uncertainties in this work is a significant improvement over our earlier analysis in Gültekin et al. (2009a). Here, we include a treatment of correlated uncertainties, which avoids a source of systematic uncertainty. We also handle multiple observations of individual objects, which increases the information provided without unduly biasing results to the particulars of an individual sources. We now mitigate the effects of contamination by XRBs on the AGN X-ray flux measurements statistically, which would produce a systematic uncertainty if we did not. We also handle non-simultaneous observations of X-ray and radio fluxes statistically to account for another source of systematic uncertainty.

3.1. Statistical Treatment

We employ emcee, the Foreman-Mackey (2016) Python implementation of MCMC, with random sampling of the data from the measurement uncertainties self-consistently for each realization. First, we describe our treatment of statistical and systematic uncertainties in our realization of the data set, and then we describe the fitting of the realized data sets.

Our strategy for treating measurement uncertainties in our fits is to use Monte Carlo methods to randomly sample each of the data points from the measurement uncertainties, keeping track of correlated uncertainties. Thus, in the maximum likelihood or MCMC methods described below, every time that we compare the data to a model, we generate a full realization of the data set. Because of the large number of data-model comparisons done in MCMC methods, we fully sample

Table 3
Spectral Fitting Results from Archival X-Ray Analysis

Galaxy	ObsID	MJD	Exposure Time ks	Net Count Rate 10^{-3} count s^{-1}	Galactic N_{H} 10^{22} cm^{-2}	Intrinsic N_{H} 10^{22} cm^{-2}	Γ	$\log F_{\text{X}}$ $\text{erg s}^{-1} \text{cm}^{-2}$	Notes
A1836-BCG	11750	55342	60	41.5	0.0498	$3.80^{+1.69}_{-1.41}$	$2.95^{+0.72}_{-0.66}$	$-13.15^{+0.10}_{-0.08}$	1
IC 2560	4908	55342	60	25.8	0.0722	...	$2.21^{+0.06}_{-0.07}$	$-12.33^{+0.02}_{-0.02}$	2
NGC 0524	6778	53976	15	1.19	0.0499	...	2	-14.30	...
NGC 1316	2022	52017	30	8.86	0.0240	$0.13^{+0.08}_{-0.06}$	$2.58^{+0.44}_{-0.37}$	$-13.70^{+0.14}_{-0.15}$...
NGC 1332	2915	52017	20	13.8	0.0222	$0.19^{+0.13}_{-0.11}$	$3.19^{+0.77}_{-0.65}$	$-13.93^{+0.19}_{-0.22}$	3
NGC 1407	791	52017	50	8.69	0.0542	$0.07^{+0.04}_{-0.04}$	$2.43^{+0.22}_{-0.21}$	$-13.75^{+0.08}_{-0.09}$...
NGC 1550	5800	53666	45	5.34	0.1020	...	2	-15.84	...
NGC 3091	3215	53666	35	1.41	0.0409	...	2	-14.43	...
NGC 3393	12290	53666	79	9.03	0.0618	...	$2.26^{+0.08}_{-0.10}$	$-12.65^{+0.03}_{-0.03}$	4
NGC 3489	392	51485	2	6.48	0.0167	...	2	$-13.68^{+0.12}_{-0.14}$...
NGC 3607	2073	51485	37	4.03	0.0136	...	2	$-13.90^{+0.05}_{-0.06}$...
NGC 3842	4189	51485	50	1.11	0.0157	...	2	$-14.61^{+0.30}_{\infty}$...
NGC 4382	2016	52059	43	1.28	0.0245	...	$1.46^{+0.45}_{-0.40}$	$-14.02^{+0.17}_{-0.18}$...
NGC 4388	12291	52059	30	93.3	0.0258	...	$1.10^{+0.01}_{-0.00}$	$-11.09^{+0.02}_{-0.02}$	5
NGC 4472	12889	55607	140	7.13	0.0153	...	$2.86^{+1.31}_{-0.78}$	$-14.71^{+0.20}_{-0.26}$	6
NGC 4477	12209	55318	10	3.11	0.0242	...	$2.90^{+0.79}_{-0.67}$	$-14.58^{+0.39}_{-0.45}$...
NGC 4486	3980	52778	5	173.5	0.0194	0.07 ± 0.02	$2.19^{+0.13}_{-0.12}$	-12.15 ± 0.05	7
NGC 4486	3981	52816	5	211.5	0.0194	0.11 ± 0.02	2.25 ± 0.12	-11.97 ± 0.05	7
NGC 4526	3925	52957	44	5.33	0.0147	...	$1.05^{+0.18}_{-0.10}$	$-13.22^{+0.06}_{-0.07}$...
NGC 4736	808	51677	50	57.9	0.0124	$0.05^{+0.01}_{-0.01}$	$2.11^{+0.07}_{-0.06}$	$-12.79^{+0.03}_{-0.03}$...
NGC 4751	12957	55666	7.5	7.84	0.0755	...	$2.50^{+0.31}_{-0.28}$	$-13.88^{+0.18}_{-0.19}$...
NGC 4826	9545	54889	28.7	7.82	0.0281	...	$3.29^{+4.92}_{-3.29}$	$-15.74^{+0.84}_{\infty}$	8
NGC 4889	13996	56013	125	5.16	0.0085	0.52	2	$-14.58^{+0.63}_{\infty}$	9
NGC 6861	11752	55057	100	5.40	0.0388	$0.05^{+0.12}_{-0.05}$	$2.19^{+0.35}_{-0.33}$	$-13.94^{+0.09}_{-0.09}$	10
NGC 7619	3955	52906	40	4.05	0.0477	...	2	$-15.08^{+0.95}_{\infty}$...

Note. This table lists X-ray spectral fits for nuclear sources from archival *Chandra* analysis. Columns list galaxy name, *Chandra* observation ID (ObsID), MJD of observation, Galactic absorption column density assumed toward each source, intrinsic absorption column density found from fits, power-law photon index, and logarithmic 2–10 keV unabsorbed flux arising from the power-law component. Uncertainties listed are 1σ , and values without uncertainties were held fixed. Fluxes without uncertainties indicate that because of low count rates the X-ray flux was estimated using PIMMS with the net count rate, assuming a $\Gamma = 2$ power law with Galactic absorption only. Such sources are treated as upper limits. We do not report intrinsic absorption column density if the best fit is less than 10^{19} cm^{-2} . The final column indicates notes as follows: (1) Fit included APEC component with $kT = 0.54$ keV, a 0.5–2 keV logarithmic flux $\log F = -13.81$ with an intrinsic absorption of $0.33 \times 10^{22} \text{ cm}^{-2}$. (2) Fit included blackbody component with $kT = 0.17$ keV and 0.5–2 keV logarithmic flux $\log F = -13.16$ and the power law comes from a pexmon spectral model with solar abundances and inclination less than 16° . (3) Fit included APEC component with $kT = 0.81$ keV, a 0.5–2 keV logarithmic flux $\log F = -13.38$. (4) Fit included blackbody component with $kT = 0.17$ keV and 0.5–2 keV logarithmic flux $\log F = -13.13$. (5) Power law comes from pexmon spectral model with abundance 1.49 and Fe abundance of 0.11 of solar with inclination fixed at 60° . The best-fit photon index is at the lower limit allowed by the pexmon model. (6) Fit included APEC component with $kT = 0.72$ keV, a 0.5–2 keV logarithmic flux $\log F = -14.24$. (7) Used results to derive average value for fundamental plane fit of $F_{\text{X}} = (8.87^{+2.33}_{-1.83}) \times 10^{-13} \text{ erg s}^{-1} \text{ cm}^{-2}$ on MJD = 52792. (8) Fit included APEC component with $kT = 0.78$ keV and a normalization of 6.98×10^{-6} at 1 keV. (9) Fit included APEC component with $kT = 0.21$ keV, a 0.5–2 keV logarithmic flux $\log F = -13.42$. We were unable to constrain the uncertainties of the intrinsic absorption. (10) Fit included APEC component with $kT = 0.97$ keV, a 0.5–2 keV logarithmic flux $\log F = -13.94$.

the measurement uncertainties and their covariances. We outline our method of Monte Carlo data realization in the following subsections.

3.1.1. Distances

For each source we assign a distance, D , drawn from the measured distance and assumed normal distribution from the given 1σ measurement uncertainty. We assume a 10% uncertainty for all extragalactic distances. Note that we use this distance for all subsequent calculations in a given realization.

3.1.2. Masses

For each source we assign a black hole mass, M , drawn from the measured black hole mass and assumed normal distribution from the given 1σ measurement uncertainty. If the high and low measurement uncertainties are asymmetric, we approximate it by averaging the two and using as the 1σ measurement uncertainty.

For AGNs, mass estimates depend on the assumed distances to the sources. To take this into account, we scale the mass to the distance realized in Section 3.1.1 linearly, except for Sgr A*, which scales as D^2 . As an example, consider NGC 3607, which has a distance $D = 22.65$ Mpc and mass $M = 1.37^{+0.45}_{-0.47} \times 10^8 M_\odot$. First we symmetrize the measurement uncertainty to be $M = (1.37 \pm 0.46) \times 10^8 M_\odot$. We simulate the mass by drawing normal deviate to be, e.g., $1.53 \times 10^8 M_\odot$. If for a given realization, the realized distance is $D = 19.15$ Mpc, then we scale the mass to $M = 1.29 \times 10^8 M_\odot$.

3.1.3. Radio Luminosities

For each source, we calculate a 5 GHz radio “luminosity” as $L_R \equiv \nu L_\nu = 5 \text{ GHz } L_5 = (5 \text{ GHz}) 4\pi D^2 F_5$, where L_5 and F_5 are the 5 GHz luminosity density and flux density, respectively, and D is the distance simulated in Section 3.1.1. Because we do not always have 5 GHz radio data, we use the following

Table 4
X-Ray Binary Sample

Source Name	Distance kpc	References	BH Mass M_{\odot}	References
4U 1543-47	7.5 ± 1.0	1	9.42 ± 0.97	2
Cygnus X-1	1.86 ± 0.12	3	14.8 ± 1.0	4
GRO J1655-40	3.2 ± 0.2	5	6.3 ± 0.25	6
GRS 1915+105	11 ± 1	7	10.1 ± 0.6	8
XTE J1118+480	1.8 ± 0.6	9	7.1 ± 1.3	10
XTE J1550-564	4.4 ± 0.5	11	9.1 ± 0.6	12

Note. This table lists the black hole X-ray binary sources used in our fundamental plane analysis. The columns indicate source name, distance to source in units of kpc, a reference code for the distance measurement, the mass of the black hole in solar units, and a reference code for the mass measurement. **References.** (1) Park et al. (2004); (2) Orosz (2003); (3) Reid et al. (2011); (4) Orosz et al. (2011a); (5) Jonker & Nelemans (2004); (6) Greene et al. (2001), where we have converted the published 95% uncertainty to a 68% value assuming a normal distribution, which is well justified by the derived probability distribution; (7) Steeghs et al. (2013); (8) Steeghs et al. (2013); (9) McClintock et al. (2001); (10) McClintock et al. (2001); (11) Orosz et al. (2011b); (12) Orosz et al. (2011b).

procedure. First, if we have 5 GHz data (as we do for eight sources), we use it. If not, we convert the $\nu \neq 5$ GHz data using a literature value for the five available measured spectral index α (using the objectively superior sign convention that $S_{\nu} \propto \nu^{-\alpha}$). The literature radio spectral index measurements are listed in Table 5 in the table notes. We simulate a value of α based on the 1σ measurement uncertainties, and use that to convert the observed F_{ν} data to F_5 . For the 13 sources for which no literature α value is available, we use additional $\nu \neq 5$ GHz data to calculate F_5 by interpolating between or extrapolating from the two F_{ν} observations, each simulated from their corresponding 1σ measurement uncertainties and assuming a power-law spectral form. The data used for these simple spectral energy distributions in the 5 GHz region are listed in Table 5 in the table notes for the sources for which it was done. Finally, if no other usable data exist (four sources), we simulate α by drawing from a uniform distribution of $[-0.5, +0.5]$ to calculate F_5 . We tried several different ranges of the uniform distribution of α and found that it had very little impact. Because we use high-angular resolution data as much as possible, we are generally insensitive to contamination from star formation at the galaxy nucleus. We note that there are two reasons to calculate α . First is to get 5 GHz flux density from measurements at other frequencies as mentioned above. Second is to determine whether the radio emission is due to core AGN activity, which would have a flat radio spectrum, or from extended jets, which would have a steep radio spectrum. We use the α estimates above for core–jet determination in Section 4.3 so that we need an estimate of α even if we have $\nu = 5$ GHz data in the same method as described above. The uncertainty of an α estimate when using two radio measurements is a combination of the uncertainties in flux densities and in the distance between the two frequencies. We assume that the uncertainty in frequency is negligibly small. While we could improve the precision of the α estimates by acquiring additional observations at other frequencies, the precision and accuracy of our estimates is sufficient for determining F_5 and for determining whether the emission is flat or steep. With two data points with arbitrarily small uncertainties in the flux density measurements, our α estimates will be very precise. As

detailed in Table 5 and as can be seen in Figure 4, most of our α estimates come from a measurement near 5 GHz and another near 8.5 or 15 GHz. This factor of ~ 2 –3 in frequency range is sufficient for our purposes.

3.1.4. X-Ray Luminosities

For each source, we calculate a 2–10 keV X-ray luminosity from the measured 2–10 keV X-ray flux, simulated from symmetrized uncertainties and converted to a luminosity using the distance simulated in Section 3.1.1. We incorporate an additional systematic uncertainty based on the non-simultaneity of radio and X-ray observations. Because we only consider XRBs with strictly or very nearly simultaneous radio and X-ray observations, we only consider this systematic uncertainty for AGNs. For radio and X-ray observations of AGNs that were taken more than 60 days apart, we include an additional 20% uncertainty. This accounts for the typical variability seen in AGNs with relatively low values of L_X/L_{Edd} as in our data set.

3.1.5. Background AGN Contamination

For extragalactic sources, we must consider the possibility that a background AGN anti-serendipitously appears at the location of our source’s nucleus. We calculate the background contamination probability as

$$P_{\text{BG}} = A_{\text{PSF}} \times \begin{cases} 5.93 \times 10^{-2} F_X^{-0.32} - 1639.51 & F_X < F_{\text{br}} \\ 4.26 \times 10^{-20} F_X^{-1.55} & F_X \geq F_{\text{br}} \end{cases}, \quad (1)$$

where $A_{\text{PSF}} = 2.424 \times 10^{-7}$ is the area of *Chandra*’s point-spread function (PSF) in square degrees, F_X is measured in units of $\text{erg s}^{-1} \text{cm}^{-2}$, and $F_{\text{br}} = 6.4 \times 10^{-15} \text{erg s}^{-1} \text{cm}^{-2}$ is the location of the break. This comes from $\log N$ – $\log S$ cumulative number density of cosmic X-ray background sources from deep field surveys (e.g., Brandt et al. 2001; Hasinger et al. 2001; Cowie et al. 2002; Rosati et al. 2002; Moretti et al. 2003; Bauer et al. 2004; Brandt & Hasinger 2005). Because of the low probabilities associated with the small value of A_{PSF} , the exact form of Equation (1) does not significantly change our results.

3.1.6. XRB Contamination

For extragalactic sources, we also need to consider contamination from low-mass X-ray binaries (LMXBs) and high-mass X-ray binaries (HMXBs) intrinsic to the galaxy near the nucleus. LMXBs tend to scale with stellar mass (M_{\star}), and HMXBs tend to scale with star formation rate (SFR) so that we consider them separately. We use the stellar masses calculated by Terrazas et al. (2016), if available; otherwise we use that calculated by van den Bosch (2016). We also calculate f_{nuc} , the fraction of total stellar light from the galaxy at the nucleus, defined by a circular radius equal to $1''$, the combined astrometric uncertainty when registering optical images usually used to determine the galaxy center, radio observations of the nucleus, and *Chandra* observations of the nucleus. We calculate this with simple photometry of Two Micron All Sky Survey or DSS images of the galaxies. The expected number of LMXBs is then given by

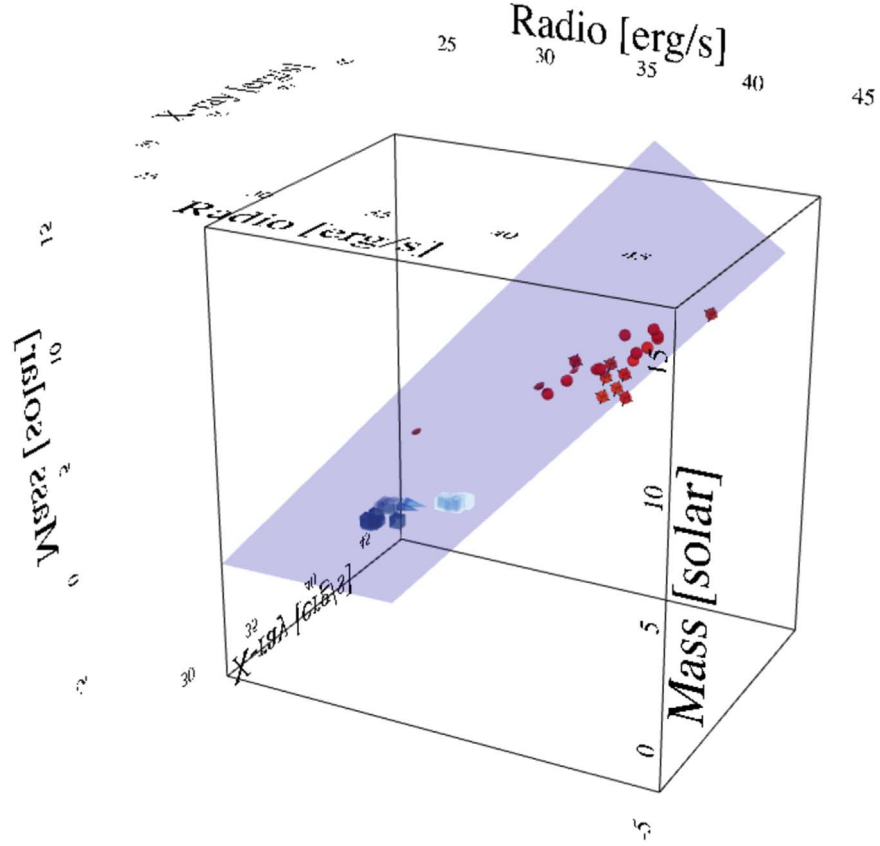


Figure 7. Three-dimensional view of the fundamental plane. The online X3D version of this figure has an interactive three-dimensional viewer to explore the data. We plot the median plane from the MCMC fits. Colors are as in Figure 6. Spheres are AGN, and spheres with axes drawn in them are Seyferts. Cubes are low/hard state XRBs, and cones are intermediate or high/soft state XRBs. The three-dimensional view of the data reveals that the data encompass a primarily planar region rather than either a line or a three-dimensional solid within the M - L_R - L_X space. This indicates that it can, in fact, be used to estimate black hole mass. The data in the interactive figure can be found in the following tables. XRB distances and masses are found in Table 4. XRB radio and X-ray fluxes are listed in Table 6. AGN data are listed in Table 5.

Kim & Fabbiano (2004) to be

$$N_{\text{LMXB}} = 25.4 f_{\text{nuc}}^* (M_*/10^{11} M_{\odot}) (L_X/10^{38} \text{ erg s}^{-1})^{-1}. \quad (2)$$

To calculate HMXB contamination, we need the SFR of each host galaxy. We use the values calculated by Terrazas et al. (2016), if available. If the source is not in Terrazas et al. (2016), we calculate SFR using the same methods from similar available far-infrared data. In particular, we estimate the SFR to be $\log(\text{SFR}/M_{\odot} \text{ yr}^{-1}) = \log(2L_{\text{FIR}}/\text{erg s}^{-1}) - 43.41$, where L_{FIR} is the far-infrared luminosity estimated from the 60 and 100 μm data as

$$\frac{F_{\text{FIR}}}{\text{erg s}^{-1} \text{ cm}^{-2}} = 1.26 \times 10^{-11} \left(2.58 \frac{S_{60}}{\text{Jy}} + \frac{S_{100}}{\text{Jy}} \right), \quad (3)$$

where F_{FIR} is the FIR flux, and S_{60} and S_{100} are the 60 and 100 μm flux densities as found in *IRAS* and other data. Because of the approximate nature involved in estimating SFR this way, we do not fold into it the distance uncertainty as the systematics of using this correlation dominate.

With the SFR estimated, we may calculate the expected number of HMXBs based on Grimm et al. (2003) to be

$$N_{\text{HMXB}} = 5.4 f_{\text{nuc}}^* (\text{SFR}/M_{\odot} \text{ yr}^{-1}) (L_X/10^{38} \text{ erg s}^{-1})^{-0.61}. \quad (4)$$

In our data set, only one of N_{LMXB} and N_{HMXB} is ever very large, and we only consider the larger of the two

to calculate the probability of XRB contamination as $P_{\text{XRB}} = 1 - \exp(-\max(N_{\text{LMXB}}, N_{\text{HMXB}}))$.

3.1.7. Censoring Data

When realizing each data set, we draw a pair of uniform random deviates from the semi-open interval $[0, 1)$ for each source. If the first random deviate is smaller than P_{BG} or the second random deviate is smaller than P_{XRB} , then we discard the given source from that realization. Thus, a source that is very unlikely to be contaminated by either XRBs or background AGNs will be represented in almost all realizations, whereas a source that has a higher chance of contamination will be represented in a smaller fraction of realizations. This allows us to consider contamination in a probabilistic way. We also discard data in which the random normal deviates used in measurement uncertainty Monte Carlo simulations result in a negative mass, radio luminosity, or X-ray luminosity. Because most of the data are detected at 3σ or better, this is not a frequent occurrence.

3.1.8. Multiple Observations of Individual Sources

As a final consideration of sources with multiple observations, primarily XRBs but also Sgr A*, we assign a weight equal to the reciprocal of the number of observations of that source that were not censored. This gives us the ability to use multiple observations as a probe of filling out the

Table 5
SMBH Sample and Radio and X-Ray Observational Data

Source	Dist. Mpc	References	M_{BH} M_{\odot}	References	MJD	ν GHz	S_{ν} mJy	References	α_R	References	MJD	F_X $\text{erg s}^{-1} \text{cm}^{-2}$	References	Notes
MGC-02-36-002	152.4	1	$3.74^{+0.42}_{-0.52} \times 10^9$	2	44239	5	440.00 ± 0.00	3	55342	$7.14^{+1.93}_{-1.19} \times 10^{-14}$	4	a,b
IC 4296	49.2	1	$1.30^{+0.20}_{-0.19} \times 10^9$	2	53280	8.46	247.70 ± 1.70	5	0.10 ± 0.24	6	52258	$5.85^{+0.46}_{-0.70} \times 10^{-13}$	7	...
Circinus	2.82	1	$1.14 \pm 0.20 \times 10^6$	8	53907	4.8	304.00 ± 15.00	9	1.13 ± 0.11	10	51617	$1.61^{+0.03}_{-0.15} \times 10^{-10}$	7	c,b
Cygnus A	242.7	1	$2.66^{+0.74}_{-0.75} \times 10^9$	11	50249	5	160.00 ± 10.00	12	51690	$2.21^{+0.11}_{-0.67} \times 10^{-11}$	7	a,c
Galaxy	0.00828	1	$4.30 \pm 0.36 \times 10^6$	13	48182	5	710.00 ± 72.00	14	1.00 ± 0.10	14	51843	$2.87^{+0.53}_{-0.39} \times 10^{-13}$	15	...
Galaxy	0.00828	1	$4.30 \pm 0.36 \times 10^6$	13	48182	5	710.00 ± 72.00	14	1.00 ± 0.10	14	51843	$1.31 \pm 0.13 \times 10^{-11}$	15	...
Galaxy	0.00828	1	$4.30 \pm 0.36 \times 10^6$	13	48182	5	710.00 ± 72.00	14	1.00 ± 0.10	14	55966	$2.51^{+0.94}_{-0.49} \times 10^{-11}$	16	...
IC 1459	28.92	1	$2.48^{+0.48}_{-0.19} \times 10^9$	17	52301	4.86	1125.70 ± 1.10	5	0.21 ± 0.02	18	52133	$6.45^{+0.19}_{-0.21} \times 10^{-13}$	7	...
IC 1481	89.9	1	$1.49^{+0.44}_{-0.45} \times 10^7$	19	51160	4.994	1.29 ± 0.15	20	3.83 ± 0.24	21	52133	a
IC 2560	37.2	1	$5.01^{+0.71}_{-0.72} \times 10^6$	22	49914	8.6	6.20 ± 0.26	23	0.90 ± 0.04	24	53052	$4.72 \pm 0.24 \times 10^{-13}$	4	c
NGC 0205	0.74	25	$<3.80 \times 10^4$	26	43431	4.885	<2.00	27	53062	$<3.90 \times 10^{-13}$	7	a,b
NGC 0221	0.805	1	$2.45^{+1.01}_{-1.02} \times 10^6$	28	56137	6.6	0.05 ± 0.01	29	-2.00 ± 1.70	29	53517	$1.71^{+0.17}_{-0.28} \times 10^{-14}$	7	...
NGC 0224	0.774	1	$1.43^{+0.91}_{-0.31} \times 10^8$	30	52485	8.4	<0.07	5	51696	$2.18^{+0.37}_{-0.65} \times 10^{-13}$	7	a
NGC 0524	24.22	1	$8.67^{+0.94}_{-0.46} \times 10^8$	31	52153	5	1.50 ± 0.09	32	0.00 ± 0.13	33	53976	$<1.58 \times 10^{-14}$	4	...
NGC 0598	0.8	25	$<3.00 \times 10^3$	34	42199	5	<1000.00	35	51786	$3.61^{+0.12}_{-0.98} \times 10^{-12}$	7	a,b
NGC 0821	23.44	1	$1.65^{+0.74}_{-0.73} \times 10^8$	36	56204	5	<0.09	37	53543	$3.58^{+0.85}_{-3.35} \times 10^{-15}$	7	a
NGC 1023	10.81	1	$4.13^{+0.43}_{-0.42} \times 10^7$	38	56204	5	<0.07	37	54276	$3.71^{+0.42}_{-0.67} \times 10^{-14}$	7	a
NGC 1068	15.9	1	$8.39 \pm 0.44 \times 10^6$	39	51429	8.46	364.00 ± 23.00	5	-0.76 ± 0.08	40	51595	$1.25^{+0.06}_{-0.08} \times 10^{-13}$	7	c
NGC 1194	57.98	1	$7.08^{+0.33}_{-0.32} \times 10^7$	41	50916	8.46	0.40 ± 0.03	42	2.51 ± 0.18	43	51595	a
NGC 1277	73	1	$1.70 \pm 0.30 \times 10^{10}$	44	51595	a
NGC 1300	21.5	1	$7.55^{+7.25}_{-3.66} \times 10^7$	45	55747	8.46	0.58 ± 0.04	46	5.74 ± 0.37	47	55115	$1.10^{+0.40}_{-0.30} \times 10^{-13}$	48	...
NGC 1316	20.95	1	$1.69^{+0.28}_{-0.30} \times 10^8$	49	50430	4.8	40.00 ± 0.10	50	1.19 ± 0.01	51	52017	$2.01^{+0.69}_{-0.60} \times 10^{-14}$	4	...
NGC 1332	22.66	1	$1.47^{+0.21}_{-0.20} \times 10^9$	52	52535	$1.19^{+0.66}_{-0.47} \times 10^{-14}$	4	a
NGC 1374	19.57	1	$5.90^{+0.61}_{-0.51} \times 10^8$	53	52535	a
NGC 1399	20.85	1	$5.04 \pm 0.69 \times 10^8$	1	45608	4.885	5.74 ± 0.72	5	51561	$<9.38 \times 10^{-16}$	7	a
NGC 1407	29	1	$4.65^{+0.73}_{-0.41} \times 10^9$	53	51772	$1.78^{+0.36}_{-0.32} \times 10^{-14}$	4	a
NGC 1550	52.5	1	$3.87^{+0.61}_{-0.71} \times 10^9$	53	51033	8.485	<0.49	5	53666	$<8.58 \times 10^{-16}$	4	a
NGC 2273	29.5	1	$8.61 \pm 0.46 \times 10^6$	41	52260	5	2.40 ± 0.20	54	-0.54 ± 0.05	40	53666	a,c
NGC 2549	12.7	1	$1.45^{+0.20}_{-1.14} \times 10^7$	31	56302	5	<0.07	37	53666	a
NGC 2748	23.4	1	$4.44^{+1.76}_{-1.82} \times 10^7$	45	55744	8.46	0.20 ± 0.05	46	55377	$7.30^{+27.50}_{-6.00} \times 10^{-16}$	48	...
NGC 2778	23.44	1	$<1.45 \times 10^7$	36	56254	5	0.11 ± 0.01	37	-0.11 ± 0.78	55	55197	$1.90^{+68.90}_{-1.80} \times 10^{-16}$	48	a
NGC 2787	7.45	1	$4.07^{+0.40}_{-0.52} \times 10^7$	56	51899	8.46	13.51 ± 0.54	5	53143	$6.80^{+0.72}_{-1.06} \times 10^{-14}$	7	...
NGC 2960	67.1	1	$1.08^{+0.04}_{-0.05} \times 10^7$	41	53143	a
NGC 3031	3.604	1	$6.50^{+2.50}_{-1.50} \times 10^7$	46	51899	8.46	153.29 ± 0.09	5	0.14 ± 0.03	40	53869	$<2.52 \times 10^{-10}$	7	a,c
NGC 3091	53.02	1	$3.72^{+0.11}_{-0.51} \times 10^9$	53	52359	$<9.83 \times 10^{-15}$	4	a
NGC 3115	9.54	1	$8.97^{+9.57}_{-2.77} \times 10^8$	57	46840	4.86	<0.33	58	52074	$8.92^{+1.28}_{-0.49} \times 10^{-15}$	7	a,b
NGC 3227	23.75	1	$2.10^{+0.69}_{-1.12} \times 10^7$	59	51922	5	4.70 ± 0.30	54	-0.90 ± 0.09	40	51542	$1.05^{+0.09}_{-0.13} \times 10^{-11}$	7	c
NGC 3245	21.38	1	$2.39^{+0.27}_{-0.76} \times 10^8$	60	53259	8.46	1.72 ± 0.15	5	52303	$3.67^{+0.41}_{-3.08} \times 10^{-14}$	7	...
NGC 3310	17.4	25	$<4.20 \times 10^7$	61	46658	4.86	2.10 ± 0.21	62	52664	$3.72^{+0.26}_{-0.90} \times 10^{-13}$	7	a
NGC 3351	8.7	25	$<8.60 \times 10^6$	63	48596	4.885	<13.50	5	53409	$<1.67 \times 10^{-10}$	7	a
NGC 3368	10.62	1	$7.66 \pm 1.53 \times 10^6$	64	50877	15	<1.00	65	51868	$5.79^{+17.41}_{-3.02} \times 10^{-16}$	7	a
NGC 3377	10.99	1	$1.78^{+0.94}_{-0.93} \times 10^8$	36	56304	5	0.19 ± 0.01	37	52645	$6.21^{+0.74}_{-4.63} \times 10^{-15}$	7	...
NGC 3379	10.7	1	$4.16 \pm 1.04 \times 10^8$	28	56304	5	0.71 ± 0.01	37	54110	$9.17^{+1.43}_{-5.05} \times 10^{-15}$	7	...
NGC 3384	11.49	1	$1.08 \pm 0.49 \times 10^7$	36	56304	5	<0.07	37	55215	$1.70^{+1.50}_{-0.80} \times 10^{-14}$	48	a

Table 5
(Continued)

Source	Dist. Mpc	References	M_{BH} M_{\odot}	References	MJD	ν GHz	S_{ν} mJy	References	α_R	References	MJD	F_X $\text{erg s}^{-1} \text{cm}^{-2}$	References	Notes
NGC 3393	49.2	1	$1.57^{+0.98}_{-0.99} \times 10^7$	66	52907	22.44	<13.20	5	55633	$2.26^{+0.16}_{-0.15} \times 10^{-13}$	4	a,c
NGC 3489	11.98	1	$5.94^{+0.84}_{-0.83} \times 10^6$	64	56266	5	<0.21	37	51485	$3.71^{+3.75}_{-2.14} \times 10^{-14}$	4	a
NGC 3585	20.51	1	$3.29^{+1.45}_{-0.58} \times 10^8$	67	52063	$1.82^{+0.27}_{-0.82} \times 10^{-14}$	7	a
NGC 3607	22.65	1	$1.37^{+0.45}_{-0.47} \times 10^8$	67	56240	5	2.05 ± 0.07	37	0.35 ± 0.10	68	52072	$1.26^{+0.16}_{-0.15} \times 10^{-14}$	4	...
NGC 3608	22.75	1	$4.65 \pm 0.99 \times 10^8$	36	56240	5	0.24 ± 0.01	37	52072	< 1.21×10^{-15}	7	a
NGC 3842	92.2	1	$9.09^{+2.31}_{-2.81} \times 10^9$	69	47498	4.835	<1.10	5	52663	< 8.90×10^{-15}	4	a
NGC 3945	19.5	1	< 8.80×10^6	67	56305	5	2.87 ± 0.09	37	0.28 ± 0.07	70	53841	$7.76^{+0.89}_{-1.48} \times 10^{-14}$	7	a
NGC 3982	18.2	25	< 8.00×10^7	63	51482	4.86	1.79 ± 0.05	40	-0.56 ± 0.06	40	53007	< 2.80×10^{-14}	7	a,c
NGC 3998	14.3	1	$8.45^{+0.70}_{-0.66} \times 10^8$	71	44216	4.885	83.00 ± 3.00	72	-0.77 ± 0.03	73	53917	$1.05 \pm 0.02 \times 10^{-11}$	7	...
NGC 4026	13.35	1	$1.80^{+0.60}_{-0.35} \times 10^8$	67	53886	< 2.78×10^{-15}	7	a
NGC 4041	20.9	25	< 6.40×10^6	74	41469	5	<41.00	75	53940	< 4.18×10^{-13}	7	a,b
NGC 4143	16.8	25	< 1.40×10^8	63	51269	4.9	8.70 ± 0.20	65	-0.12 ± 0.03	76	51994	$2.68^{+238.32}_{-1.95} \times 10^{-13}$	7	a
NGC 4203	16	25	< 3.80×10^7	63	50877	15	9.00 ± 0.23	65	0.44 ± 0.04	40	51486	$8.17^{+0.96}_{-1.61} \times 10^{-13}$	7	a
NGC 4258	7.27	1	$3.78 \pm 0.04 \times 10^7$	46	51899	8.46	2.88 ± 0.10	5	-0.18 ± 0.03	40	52058	$1.12^{+0.09}_{-0.35} \times 10^{-11}$	7	c
NGC 4261	32.36	1	$5.29^{+1.07}_{-1.08} \times 10^8$	77	49479	4.885	285.00 ± 2.77	78	1.92 ± 0.03	79	54508	$7.74^{+0.42}_{-0.58} \times 10^{-13}$	7	...
NGC 4291	26.58	1	$9.78^{+3.12}_{-3.08} \times 10^8$	36	55724	8.46	<0.14	46	55541	$1.40^{+0.60}_{-0.40} \times 10^{-14}$	48	a
NGC 4321	18	25	< 2.70×10^7	63	52201	5	0.53 ± 0.06	80	51488	< 4.34×10^{-15}	7	a
NGC 4342	22.91	1	$4.53^{+2.65}_{-1.48} \times 10^8$	81	46778	4.86	<0.50	82	53412	$3.54^{+0.59}_{-1.48} \times 10^{-14}$	7	a,b
NGC 4374	18.51	1	$9.25^{+0.95}_{-0.87} \times 10^8$	83	51269	4.9	160.00 ± 0.20	65	0.17 ± 0.02	84	51683	< 6.78×10^{-11}	7	a
NGC 4382	17.88	1	< 1.30×10^7	85	52059	$9.45^{+4.45}_{-3.14} \times 10^{-15}$	4	a
NGC 4388	16.53	1	$7.31^{+0.17}_{-0.18} \times 10^6$	41	50877	15	3.70 ± 0.09	54	-0.80 ± 0.08	40	55902	$8.21^{+0.35}_{-0.33} \times 10^{-12}$	4	c
NGC 4435	17	25	< 8.00×10^6	86	56303	5	0.12 ± 0.01	37	54507	< 7.53×10^{-11}	7	a
NGC 4459	16.01	1	$6.96^{+1.33}_{-1.34} \times 10^7$	56	56303	5	0.37 ± 0.03	37	-0.21 ± 0.20	87	55310	$2.30^{+0.30}_{-0.70} \times 10^{-14}$	48	...
NGC 4472	16.72	1	$2.54^{+0.58}_{-0.10} \times 10^9$	53	51269	4.9	2.30 ± 0.20	65	-0.45 ± 0.05	40	55607	$1.95^{+1.11}_{-0.89} \times 10^{-15}$	4	...
NGC 4473	15.25	1	$9.00 \pm 4.50 \times 10^7$	36	56303	5	<0.15	37	53427	< 7.09×10^{-15}	7	a
NGC 4477	18	25	< 8.40×10^7	56	56279	5.5	0.12 ± 0.02	5	55318	$2.65^{+3.87}_{-1.72} \times 10^{-15}$	4	a,c
NGC 4486	16.68	1	$6.15^{+0.38}_{-0.37} \times 10^9$	88	52793	8.435	2803.00 ± 15.00	5	0.19 ± 0.01	89	52797	$8.87^{+2.33}_{-1.83} \times 10^{-13}$	72	...
NGC 4486A	18.36	1	$1.44^{+0.53}_{-0.52} \times 10^7$	91	55737	8.394	<0.00	46	55299	$4.00^{+4.30}_{-2.40} \times 10^{-15}$	48	a
NGC 4486B	16.26	1	$6.00^{+3.00}_{-2.00} \times 10^8$	92	53842	8.4	<0.15	93	52964	$2.96^{+0.66}_{-1.71} \times 10^{-15}$	7	a
NGC 4501	18	25	< 7.90×10^7	63	51482	4.86	1.14 ± 0.06	40	-0.48 ± 0.05	40	52617	$3.93^{+0.70}_{-1.62} \times 10^{-14}$	7	a,c
NGC 4526	16.44	1	$4.51^{+1.40}_{-1.03} \times 10^8$	94	56302	5	1.48 ± 0.05	37	52957	$6.08^{+0.85}_{-0.88} \times 10^{-14}$	4	...
NGC 4548	20.3	25	< 3.40×10^7	63	50877	15	1.60 ± 0.04	65	51992	< 3.03×10^{-13}	7	a
NGC 4564	15.94	1	$8.81^{+2.49}_{-2.43} \times 10^7$	36	56303	5	<0.09	37	52964	$1.86^{+0.39}_{-1.48} \times 10^{-14}$	7	a
NGC 4594	9.87	1	$6.65^{+0.40}_{-0.41} \times 10^8$	95	53280	8.46	59.90 ± 2.20	5	52060	$1.23^{+0.15}_{-0.89} \times 10^{-12}$	7	...
NGC 4596	16.53	1	$7.67^{+3.73}_{-3.24} \times 10^7$	56	56302	5	<0.10	37	55151	$3.90^{+4.30}_{-2.20} \times 10^{-15}$	48	a
NGC 4649	16.46	1	$4.72^{+1.04}_{-1.05} \times 10^9$	96	50888	8.46	18.45 ± 0.32	5	1.52 ± 0.01	97	54130	< 1.72×10^{-14}	7	a
NGC 4697	12.54	1	$2.02^{+0.51}_{-0.50} \times 10^8$	36	56306	5	<0.07	37	51558	$9.74^{+2.56}_{-9.34} \times 10^{-15}$	7	a
NGC 4698	18	25	< 7.60×10^7	56	51482	4.86	0.23 ± 0.06	40	52441	$1.71^{+0.24}_{-0.61} \times 10^{-14}$	7	a,c
NGC 4736	5	1	$6.77 \pm 1.56 \times 10^6$	98	49479	4.885	4.00 ± 0.22	78	0.76 ± 0.09	99	51677	$1.62^{+0.11}_{-0.10} \times 10^{-13}$	4	...
NGC 4742	16.4	100	$1.40^{+0.40}_{-0.50} \times 10^7$	101	55735	8.46	<0.00	46	55160	$2.50^{+0.80}_{-0.60} \times 10^{-14}$	48	a
NGC 4751	32.81	1	$2.44^{+0.12}_{-0.37} \times 10^9$	53	55666	$1.30^{+0.66}_{-0.47} \times 10^{-14}$	4	a
NGC 4826	7.27	1	$1.56 \pm 0.39 \times 10^6$	98	50877	15	<0.90	54	54889	< 7.85×10^{-15}	4	a
NGC 4889	102	1	$2.08^{+1.58}_{-1.59} \times 10^{10}$	69	47593	4.86	<2.70	5	56013	< 2.62×10^{-14}	4	a
NGC 4945	3.58	1	$1.35^{+0.68}_{-0.48} \times 10^6$	102	49133	4.998	297.00 ± 0.03	103	-0.60 ± 0.06	103	51570	< 2.25×10^{-12}	7	a,c

Table 5
(Continued)

Source	Dist. Mpc	References	M_{BH} M_{\odot}	References	MJD	ν GHz	S_{ν} mJy	References	α_R	References	MJD	F_X erg s $^{-1}$ cm $^{-2}$	References	Notes
NGC 5077	38.7	1	$8.55^{+4.35}_{-4.48} \times 10^8$	104	55742	8.46	193.10 ± 5.80	46	0.32 ± 0.07	105	55325	$2.80^{+0.90}_{-0.70} \times 10^{-14}$	48	...
NGC 5128	3.62	1	$5.69 \pm 1.04 \times 10^7$	106	53353	8.46	4700.00 ± 250.00	5	0.33 ± 0.06	107	52896	$7.15^{+0.74}_{-1.81} \times 10^{-12}$	7	...
NGC 5516	55.3	1	$3.69^{+0.10}_{-1.04} \times 10^9$	52	52862	a
NGC 5576	25.68	1	$2.73^{+0.68}_{-0.79} \times 10^8$	67	56302	5	<0.09	37	55342	$2.70^{+5.60}_{-1.80} \times 10^{-15}$	48	a
NGC 5845	25.87	1	$4.87 \pm 1.53 \times 10^8$	36	56302	5	<0.07	37	52642	$1.21^{+0.13}_{-0.16} \times 10^{-14}$	7	a
NGC 6086	138	1	$3.74^{+1.76}_{-1.15} \times 10^9$	108	54542	5	<0.55	109	52642	a
NGC 6251	108.4	1	$6.14^{+2.04}_{-2.05} \times 10^8$	110	51679	4.9891	380.00 ± 0.40	111	-0.02 ± 0.09	112	52954	$<6.06 \times 10^{-12}$	7	a
NGC 6264	147.6	1	$3.08 \pm 0.04 \times 10^7$	41	52954	a
NGC 6323	113.4	1	$1.01^{+0.02}_{-0.01} \times 10^7$	41	52954	a
NGC 6861	28.71	1	$2.10^{+0.63}_{-0.10} \times 10^9$	53	55057	$1.15^{+0.26}_{-0.22} \times 10^{-14}$	4	a
NGC 7052	70.4	1	$3.96^{+2.76}_{-1.56} \times 10^8$	113	50907	8.46	47.53 ± 0.56	5	52538	$<1.45 \times 10^{-14}$	7	a
NGC 7457	12.53	1	$9.00^{+5.30}_{-5.40} \times 10^6$	36	56234	5	<0.07	37	55085	$4.30^{+16.00}_{-3.40} \times 10^{-15}$	48	a
NGC 7582	22.3	1	$5.51^{+1.30}_{-0.95} \times 10^7$	114	45149	4.86	69.00 ± 1.25	115	0.71 ± 0.02	116	51831	$8.21^{+1.04}_{-4.66} \times 10^{-12}$	7	...
NGC 7619	53.85	1	$2.30^{+1.15}_{-0.11} \times 10^9$	53	46049	4.89	1.92 ± 0.12	5	1.66 ± 0.05	117	52906	$<5.07 \times 10^{-14}$	4	a
NGC 7768	116	1	$1.34^{+0.51}_{-0.41} \times 10^9$	69	54512	5	0.72 ± 0.09	109	52906	a
UGC 3789	49.9	1	$9.65 \pm 1.55 \times 10^6$	118	54791	8.435	<5.40	5	52906	a
UGC 9799	151.1	25	$<4.90 \times 10^9$	2	51242	4.9	345.00 ± 14.00	119	0.88 ± 0.11	120	51790	$<1.24 \times 10^{-13}$	7	a

Notes. This table shows the SMBH data we use in our fundamental plane analysis. The columns provide source name, distance in units of Mpc, a reference code for the distance measurement, the mass of the black hole in solar units, a reference code for the mass measurement, the MJD of the radio observation, the frequency of the radio observation, the core radio flux density, a reference code for the radio observation, the MJD of the X-ray observation, the 2–10 keV X-ray flux, a reference code for the X-ray measurement.

^a Did not use in fundamental plane analysis.

^b Radio data comes from observation with large beam and therefore may contain emission that is not solely core AGN emission.

^c Seyfert.

References. (1) Kormendy & Ho (2013); (2) Dalla Bontà et al. (2009); (3) Wright & Otrupcek (1990); (4) our analysis of archival *Chandra* data (Section C); (5) our analysis of archival VLA data (Section B); (6) from $S_5 = 262 \pm 34$ mJy (Murphy et al. 2010); (7) Gültekin et al. (2009a); (8) Greenhill et al. (2003); (9) Murphy et al. (2010); (10) from $S_{8.64} = 156 \pm 7$ mJy (Murphy et al. 2010); (11) Tadhunter et al. (2003); (12) Hirabayashi et al. (2000); (13) Genzel et al. (2010); (14) Zhao et al. (2001); (15) Baganoff et al. (2001); (16) Nowak et al. (2012); (17) Cappellari et al. (2002); (18) from $S_{8.4} = 1001.5 \pm 13$ mJy (Healey et al. 2007); (19) Huré (2002); (20) Xanthopoulos et al. (2010); (21) from $S_{2.38} = 22 \pm 3$ mJy (Dressel & Condon 1978); (22) Yamauchi et al. (2012); (23) Morganti et al. (1999); (24) from $S_{1.4} = 32 \pm 1.7$ mJy (Condon et al. 1998); (25) Gültekin et al. (2009c); (26) Valluri et al. (2005); (27) Heckman et al. (1980); (28) van den Bosch & de Zeeuw (2010); (29) Yang et al. (2015); (30) Bender et al. (2005); (31) Krajnović et al. (2009); (32) Filho et al. (2004); (33) from $S_{15} = 1.5 \pm 0.2$ mJy (Nagar et al. 2005); (34) Gebhardt et al. (2001); (35) Merritt et al. (2001); (36) Schulze & Gebhardt (2011); (37) Nyland et al. (2016); (38) Bower et al. (2001); (39) Lodato & Bertin (2003); Huré (2002); (40) Ho & Ulvestad (2001); (41) Kuo et al. (2011); (42) Schmitt et al. (2001); (43) from $S_5 = 1.5 \pm 0.083$ mJy (Gallimore et al. 2006); (44) van den Bosch et al. (2012); (45) Atkinson et al. (2005); (46) our analysis of new EVLA data (Section A); (47) from $S_5 = 11 \pm 2$ mJy (Beck et al. 2002); (48) Gültekin et al. (2012); (49) Nowak et al. (2008); (50) Tingay et al. (2003); (51) from $S_{8.6} = 20 \pm 0.1$ mJy (Tingay et al. 2003); (52) Rusli et al. (2011); (53) Rusli et al. (2013); (54) Nagar et al. (2005); (55) Sarzi et al. (2001); (56) Emsellem et al. (1999); (57) Fabbiano et al. (1989); (58) Davies et al. (2006); (59) Barth et al. (2001); (60) Pastorini et al. (2007); (61) Saikia et al. (1994); (62) Sarzi et al. (2002); (63) Nowak et al. (2010); (64) Nagar et al. (2002); (65) Kondratko et al. (2008); Huré et al. (2011); (66) Gültekin et al. (2009b); (67) from $S_{15} = 1.4 \pm 0.15$ mJy (Nagar et al. 2005); (68) McConnell et al. (2012); (69) from $S_{15} = 2.1 \pm 0.15$ mJy (Nagar et al. 2005); (70) Walsh et al. (2012); (71) Wrobel & Heeschen (1984); (72) from $S_{15} = 196 \pm 3$ mJy (Richards et al. 2011); (73) Marconi et al. (2003); (74) Sramek (1975); (75) from $S_{15} = 10 \pm 0.25$ mJy (Nagar et al. 2002); (76) Ferrarese et al. (1996); (77) Laurent-Muehleisen et al. (1997); (78) from $S_{8.387} = 101 \pm 1$ mJy (Jones & Wehrle 1997); (79) Filho et al. (2006); (80) Cretton & van den Bosch (1999); (81) Wrobel & Heeschen (1991); (82) Walsh et al. (2010); (83) from $S_{8.46} = 146 \pm 1.3$ mJy from our analysis of archival VLA data (Section B); (84) Gebhardt et al. (2011); (85) Gültekin et al. (2011); (86) Coccato et al. (2006); (87) from $S_{8.394} = 0.452 \pm 0.028$ mJy from our analysis of archival VLA data (Section B); (88) Gebhardt et al. (2011); (89) from $S_5 = 3097.1 \pm 0.1$ mJy (Nagar et al. 2001); (90) Nowak et al. (2007); (91) Kormendy et al. (1997); (92) Capetti et al. (2009); (93) Davis et al. (2013); (94) Jardel et al. (2011); (95) Shen & Gebhardt (2010); (96) from $S_{1.4} = 282 \pm 0.03$ mJy (Shurkin et al. 2008); (97) K. Gebhardt et al. (2018, in preparation); (98) from $S_{15} = 1.7 \pm 0.15$ mJy (Nagar et al. 2005); (99) Tonry et al. (2001); (100) K. Gültekin et al. (2018, in preparation); (101) Greenhill et al. (1997); (102) Elmoutie et al. (1997); (103) de Francesco et al. (2008); (104) from $S_{20} = 149 \pm 8$ mJy (Murphy et al. 2010); (105) Cappellari et al. (2009); (106) from $S_{22.3} = 3400 \pm 100$ mJy (Müller et al. 2011); (107) Müller et al. (2011); (108) McConnell et al. (2011); (109) Liuzzo et al. (2010); (110) Ferrarese & Ford (1999); (111) Evans et al. (2005); (112) from $S_{15} = 390 \pm 40$ mJy (Evans et al. 2005); (113) van der Marel & van den Bosch (1998); (114) Wold et al. (2006); (115) Ulvestad & Wilson (1984); (116) from $S_{1.4} = 166 \pm 2$ mJy (Ulvestad & Wilson 1984); (117) from $S_{1.4} = 15.4 \pm 0.123$ mJy (White et al. 1997); (118) Kuo et al. (2011); Huré et al. (2011); (119) Venturi et al. (2004); (120) from $S_{8.3} = 217 \pm 9$ mJy (Venturi et al. 2004).

Table 6
X-Ray Binary Radio and X-Ray Observational Data

Source	Radio Obs.	Radio MJD	ν GHz	S_ν mJy	References	X-Ray Obs.	X-Ray MJD	F_X $10^{-10} \text{ erg s}^{-1} \text{ cm}^{-2}$	References	State	References	Notes
4U 1543-47	ATCA	52445	4.8	3.18 ± 0.19	1	<i>RXTE</i>	52445.6	58.30 ± 1.20	2	Very high	1	a
4U 1543-47	ATCA	52490	4.8	4.00 ± 0.05	1	<i>RXTE</i>	52490.1	0.88 ± 0.01	2	Low/hard	1	a
Cyg X-1	AMI	54928	15	9.30 ± 0.20	3	<i>Suzaku</i>	54925.4	100.00 ± 2.60	3	Low/hard	3	b
Cyg X-1	AMI	54933	15	11.60 ± 0.10	3	<i>Suzaku</i>	54930.4	79.60 ± 2.40	3	Low/hard	3	b
Cyg X-1	AMI	54940	15	8.80 ± 0.10	3	<i>Suzaku</i>	54936.4	67.30 ± 2.00	3	Low/hard	3	b
Cyg X-1	AMI	54945	15	10.80 ± 0.10	3	<i>Suzaku</i>	54945.4	70.00 ± 2.10	3	Low/hard	3	b
Cyg X-1	AMI	54953	15	10.20 ± 0.20	3	<i>Suzaku</i>	54950.4	74.10 ± 2.20	3	Low/hard	3	b
Cyg X-1	AMI	54958	15	9.60 ± 0.10	3	<i>Suzaku</i>	54958.4	89.10 ± 2.70	3	Low/hard	3	b
Cyg X-1	AMI	54971	15	13.50 ± 0.10	3	<i>Suzaku</i>	54972.4	85.30 ± 2.50	3	Low/hard	3	b
Cyg X-1	AMI	54983	15	14.70 ± 0.20	3	<i>Suzaku</i>	54977.4	111.00 ± 3.00	3	Low/hard	3	b
Cyg X-1	AMI	54983	15	14.70 ± 0.20	3	<i>Suzaku</i>	54981.4	116.00 ± 3.00	3	Low/hard	3	b
Cyg X-1	AMI	54987	15	19.60 ± 0.10	3	<i>Suzaku</i>	54985.4	121.00 ± 4.00	3	Low/hard	3	b
Cyg X-1	AMI	54987	15	19.60 ± 0.10	3	<i>Suzaku</i>	54987.4	115.00 ± 3.00	3	Low/hard	3	b
Cyg X-1	AMI	55126	15	9.40 ± 0.80	3	<i>Suzaku</i>	55126.4	68.90 ± 2.10	3	Low/hard	3	b
Cyg X-1	AMI	55131	15	6.50 ± 0.10	3	<i>Suzaku</i>	55131.4	68.60 ± 2.00	3	Low/hard	3	b
Cyg X-1	AMI	55142	15	7.20 ± 0.30	3	<i>Suzaku</i>	55139.4	52.70 ± 1.50	3	Low/hard	3	b
Cyg X-1	AMI	55147	15	6.10 ± 0.20	3	<i>Suzaku</i>	55146.4	46.10 ± 1.30	3	Low/hard	3	b
Cyg X-1	AMI	55153	15	6.00 ± 0.10	3	<i>Suzaku</i>	55153.4	103.00 ± 3.00	3	Low/hard	3	b
Cyg X-1	AMI	55161	15	13.30 ± 0.20	3	<i>Suzaku</i>	55160.4	81.80 ± 2.40	3	Low/hard	3	b
Cyg X-1	AMI	55167	15	13.60 ± 0.10	3	<i>Suzaku</i>	55167.4	76.60 ± 2.30	3	Low/hard	3	b
Cyg X-1	AMI	55176	15	16.20 ± 0.20	3	<i>Suzaku</i>	55174.4	79.10 ± 2.40	3	Low/hard	3	b
Cyg X-1	AMI	55188	15	15.30 ± 0.50	3	<i>Suzaku</i>	55183.4	143.00 ± 5.00	3	Low/hard	3	b
GRO J1655-40	VLA B	53425	4.86	1.46 ± 0.07	4	<i>RXTE</i>	53424.0	2.07 ± 0.04	2	Low/hard	4	...
GRO J1655-40	VLA B	53426	4.86	1.52 ± 0.11	4	<i>RXTE</i>	53425.1	2.56 ± 0.05	2	Low/hard	4	...
GRO J1655-40	VLA B	53429	4.86	1.86 ± 0.06	4	<i>RXTE</i>	53429.0	4.02 ± 0.05	2	Low/hard	4	...
GRO J1655-40	VLA B	53434	4.86	2.01 ± 0.10	4	<i>RXTE</i>	53434.0	5.69 ± 0.13	2	Low/hard	4	...
GRS 1915+105	GBI	50584	5	28.56 ± 4.14	5	<i>RXTE</i>	50583.5	181.00 ± 18.00	5	Hard-steady	5	c
GRS 1915+105	GBI	50725	5	156.11 ± 6.55	5	<i>RXTE</i>	50724.9	593.00 ± 60.00	5	Hard-steady	5	c
GRS 1915+105	GBI	50729	5	26.00 ± 4.45	5	<i>RXTE</i>	50729.3	247.00 ± 25.00	5	Hard-steady	5	c
GRS 1915+105	GBI	50730	5	38.25 ± 4.20	5	<i>RXTE</i>	50730.4	230.00 ± 23.00	5	Hard-steady	5	c
GRS 1915+105	GBI	50736	5	58.72 ± 3.88	5	<i>RXTE</i>	50735.6	130.00 ± 13.00	5	Hard-steady	5	c
GRS 1915+105	GBI	50737	5	63.45 ± 3.58	5	<i>RXTE</i>	50737.4	139.00 ± 14.00	5	Hard-steady	5	c
GRS 1915+105	GBI	50743	5	56.37 ± 3.77	5	<i>RXTE</i>	50743.3	144.00 ± 15.00	5	Hard-steady	5	c
GRS 1915+105	GBI	50746	5	42.74 ± 4.09	5	<i>RXTE</i>	50746.3	153.00 ± 15.00	5	Hard-steady	5	c
GRS 1915+105	GBI	50910	5	85.44 ± 3.91	5	<i>RXTE</i>	50909.9	210.00 ± 21.00	5	Hard-steady	5	c
GRS 1915+105	GBI	50913	5	85.55 ± 3.96	5	<i>RXTE</i>	50912.9	230.00 ± 23.00	5	Hard-steady	5	c
GRS 1915+105	GBI	50913	5	85.67 ± 3.98	5	<i>RXTE</i>	50913.0	234.00 ± 23.00	5	Hard-steady	5	c
GRS 1915+105	GBI	50923	5	111.09 ± 5.29	5	<i>RXTE</i>	50923.3	440.00 ± 44.00	5	Hard-steady	5	c
GRS 1915+105	GBI	50926	5	111.60 ± 4.28	5	<i>RXTE</i>	50925.9	207.00 ± 21.00	5	Hard-steady	5	c
GRS 1915+105	GBI	50932	5	98.64 ± 4.32	5	<i>RXTE</i>	50931.7	183.00 ± 19.00	5	Hard-steady	5	c
GRS 1915+105	GBI	50939	5	126.56 ± 4.86	5	<i>RXTE</i>	50938.9	163.00 ± 16.00	5	Hard-steady	5	c
GRS 1915+105	GBI	50945	5	79.89 ± 3.88	5	<i>RXTE</i>	50944.9	198.00 ± 20.00	5	Hard-steady	5	c
GRS 1915+105	GBI	50945	5	80.01 ± 3.79	5	<i>RXTE</i>	50945.0	190.00 ± 19.00	5	Hard-steady	5	c
GRS 1915+105	GBI	50945	5	79.78 ± 3.82	5	<i>RXTE</i>	50945.1	189.00 ± 19.00	5	Hard-steady	5	c
GRS 1915+105	GBI	50945	5	80.17 ± 3.82	5	<i>RXTE</i>	50945.2	187.00 ± 19.00	5	Hard-steady	5	c
GRS 1915+105	GBI	50953	5	96.61 ± 4.05	5	<i>RXTE</i>	50952.6	152.00 ± 15.00	5	Hard-steady	5	c

Table 6
(Continued)

Source	Radio Obs.	Radio MJD	ν GHz	S_ν mJy	References	X-Ray Obs.	X-Ray MJD	F_X $10^{-10} \text{ erg s}^{-1} \text{ cm}^{-2}$	References	State	References	Notes
GRS 1915+105	GBI	50958	5	51.19 ± 4.08	5	<i>RXTE</i>	50957.8	136.00 ± 14.00	5	Hard-steady	5	^c
GRS 1915+105	GBI	50965	5	48.11 ± 4.23	5	<i>RXTE</i>	50964.8	191.00 ± 19.00	5	Hard-steady	5	^c
GRS 1915+105	GBI	50975	5	68.81 ± 5.01	5	<i>RXTE</i>	50975.3	186.00 ± 19.00	5	Hard-steady	5	^c
GRS 1915+105	GBI	50981	5	57.47 ± 5.07	5	<i>RXTE</i>	50980.8	246.00 ± 25.00	5	Hard-steady	5	^c
GRS 1915+105	GBI	50992	5	32.77 ± 4.86	5	<i>RXTE</i>	50991.6	168.00 ± 17.00	5	Hard-steady	5	^c
GRS 1915+105	GBI	50992	5	32.93 ± 4.63	5	<i>RXTE</i>	50991.7	167.00 ± 17.00	5	Hard-steady	5	^c
GRS 1915+105	GBI	51002	5	47.68 ± 5.64	5	<i>RXTE</i>	51002.2	138.00 ± 14.00	5	Hard-steady	5	^c
GRS 1915+105	GBI	51002	5	47.82 ± 5.50	5	<i>RXTE</i>	51002.2	148.00 ± 15.00	5	Hard-steady	5	^c
GRS 1915+105	GBI	51003	5	128.39 ± 5.06	5	<i>RXTE</i>	51003.2	250.00 ± 25.00	5	Hard-steady	5	^c
GRS 1915+105	GBI	51004	5	198.77 ± 7.88	5	<i>RXTE</i>	51004.4	486.00 ± 48.00	5	Hard-steady	5	^c
GRS 1915+105	GBI	51005	5	72.55 ± 5.82	5	<i>RXTE</i>	51005.2	303.00 ± 30.00	5	Hard-steady	5	^c
GRS 1915+105	GBI	51006	5	53.88 ± 5.56	5	<i>RXTE</i>	51006.2	202.00 ± 20.00	5	Hard-steady	5	^c
GRS 1915+105	GBI	51006	5	53.64 ± 5.36	5	<i>RXTE</i>	51006.2	183.00 ± 18.00	5	Hard-steady	5	^c
GRS 1915+105	GBI	51057	5	32.12 ± 4.53	5	<i>RXTE</i>	51056.8	206.00 ± 20.00	5	Hard-steady	5	^c
GRS 1915+105	GBI	51194	5	25.75 ± 3.82	5	<i>RXTE</i>	51194.0	125.00 ± 13.00	5	Hard-steady	5	^c
GRS 1915+105	GBI	51221	5	65.87 ± 4.08	5	<i>RXTE</i>	51221.1	219.00 ± 22.00	5	Hard-steady	5	^c
XTE J1118+480	Ryle	51634	15	6.20 ± 0.50	6	<i>RXTE</i>	51634.0	7.55 ± 0.08	2	Low/hard	7	^d
XTE J1118+480	Ryle	51637	15	7.50 ± 0.30	8	<i>RXTE</i>	51636.2	7.97 ± 0.08	2	Low/hard	7	^d
XTE J1118+480	VLA C	51637	8.3	6.00 ± 0.10	8	<i>RXTE</i>	51637.0	7.86 ± 0.08	2	Low/hard	7	^d
XTE J1550-564	ATCA	51665	4.8	7.45 ± 0.12	9	<i>RXTE</i>	51664.4	57.80 ± 1.00	2	Int./very high	9	^e
XTE J1550-564	ATCA	51697	4.8	0.88 ± 0.08	9	<i>RXTE</i>	51696.5	3.86 ± 0.03	2	Low/hard	9	^e

Notes. This table shows the X-ray binary data we use in our fundamental plane analysis. Columns indicate the source, the radio observatory used, MJD of the radio observation, frequency of the radio observation in GHz, flux density of the radio observation in mJy, the reference code for the radio observation, the X-ray observatory used, the MJD of the X-ray observation, the 2–10 keV flux, the reference code for the X-ray data, the state of the source, and the reference code for the state identification.

^a Radio spectral index measurements of $\alpha = -0.24$ and 0.08 for the first and second data, respectively (Kalemci et al. 2005).

^b X-ray data were converted from published 0.8–10 keV band to 2–10 keV band using PIMMS.

^c Radio data interpolated between 2.25 and 8.3 GHz.

^d Radio spectral index measurement of $\alpha = 0.5$ for the first datum only (Fender et al. 2001).

^e Radio spectral index measurements of $\alpha = -0.46$ and 0.37 for the first and second data, respectively (Corbel et al. 2001).

References. (1) Kalemci et al. (2005); (2) our analysis of archival X-ray data; (3) Miller et al. (2012); (4) Shaposhnikov et al. (2007); (5) Munro et al. (2001); (6) Pooley & Waldram (2000); (7) Fender et al. (2001); (8) Dhawan et al. (2000); (9) Corbel et al. (2001).

fundamental plane if, e.g., an XRB is observed at vastly different regions of the L_R - L_X plane without over-weighting a source that happens to have many observations.

3.2. MCMC Fitting

We use the following model, describing the plane

$$\mu = \mu_0 + \xi_{\mu R}R + \xi_{\mu X}X, \quad (5)$$

where $\mu \equiv \log(M/10^8 M_\odot)$, $R \equiv \log(L_R/10^{38} \text{ erg s}^{-1})$, and $X \equiv \log(L_X/10^{40} \text{ erg s}^{-1})$. The model parameters are the mass intercept (μ_0), radio slope ($\xi_{\mu R}$), X-ray slope ($\xi_{\mu X}$), and a Gaussian intrinsic scatter in the log-mass direction (ϵ_μ). In our fitting, we first find the maximum likelihood model by minimizing the negative of the following likelihood:

$$\log \mathcal{L} = -\frac{1}{2} \sum_{i=1}^N w_i (\mu_i - \mu(R_i, X_i, \theta))^2 \epsilon_\mu^{-2} + \log \epsilon_\mu^2, \quad (6)$$

where w_i is a weight for each of the N data points (μ_i , R_i , X_i) and θ is a vector of the model parameters. In practice, we use $\ln \epsilon_\mu$ as a fit parameter to avoid numerical problems associated with negative values of ϵ_μ in minimization techniques.

We use the results of the maximum likelihood finding as a starting location with the Foreman-Mackey (2016) implementation of the Goodman & Weare (2010) affine-invariant MCMC ensemble sampler. We start 100 walkers in a small region centered on the maximum likelihood results randomized in each parameter with a small (10^{-4}) deviation for each of the walkers. For all model parameters (μ_0 , $\xi_{\mu R}$, $\xi_{\mu X}$, and $\ln \epsilon_\mu$) we use an uninformative uniform prior of $(-5, +5)$. Tests with different priors showed no differences to the results. We ran the sampler for different numbers of steps, inspecting the chains visually to determine how many steps should be used for burn-in. We found that 200 steps was always sufficient for burn-in. We tried various numbers of steps, up to 10^6 to ensure robust results. These experiments showed that any number of steps above 10 times the autocorrelation time gave essentially the same median and 68% interval, and the only merit in increasing the number of steps above was smoother posterior figures. Thus, we present results with 10^6 steps to show the smoothest figures.

3.3. Fitting Results

The results of our MCMC fitting are summarized in Figure 5. We take the median and 68% interval of the posterior distribution as our final results. Our best fitting correlation parameters are

$$\begin{aligned} \mu_0 &= 0.55 \pm 0.22, \\ \xi_{\mu R} &= 1.09 \pm 0.10, \\ \xi_{\mu X} &= -0.59_{-0.15}^{+0.16}, \text{ and} \\ \ln \epsilon_\mu &= -0.04_{-0.13}^{+0.14}. \end{aligned} \quad (7)$$

The posterior probability distributions are singly peaked with a roughly normal distribution, indicating robust results.

Our results are also summarized in Figure 6, which shows the edge-on projection of the fundamental plane with $\log M$ as the dependent variable. The figure shows no apparent residual trend with Eddington fraction, nor do the non-low/hard state XRBs appear to be outliers. There is, however, substantial

intrinsic scatter of $\epsilon_\mu \approx 1$ dex, indicating a large amount of unexplained variance. The edge-on projection shows XRBs to be low compared to the projected median relation. As seen in the three-dimensional views in Figure 7, this offset cannot be fixed by a simple adjustment of a slope in the edge-on projection.

4. Discussion

In Section 3.3 we found the best-fit mass-predictor relation for our full sample to be

$$\mu = 0.55 \pm 0.22 + (1.09 \pm 0.10)R + (-0.59_{-0.15}^{+0.16})X, \quad (8)$$

with an intrinsic scatter of $\ln \epsilon_\mu = -0.04_{-0.13}^{+0.14}$. Here we consider alternative samples from our parent full sample and comment on the implications. In Section 4.8, we compare the differences between this work and our earlier results in Gültekin et al. (2009a).

4.1. Sgr A*

As the source with the lowest L_X/L_{Edd} value, Sgr A* deserves special consideration that its accretion properties may be different from the rest as it would be undetectable outside the Local Group. Sgr A* is listed in Table 5 three times for three different X-ray states. It has been argued previously that Sgr A* only approaches the fundamental plane during its X-ray flare state (Plotkin et al. 2012). To investigate this, we try fitting the fundamental plane using only the brightest X-ray flux from MJD = 51843. When doing so, the best-fit relation becomes

$$\mu = 0.53_{-0.23}^{+0.22} + (1.08 \pm 0.11)R + (-0.56 \pm 0.18)X, \quad (9)$$

with an intrinsic scatter of $\ln \epsilon_\mu = -0.02_{-0.14}^{+0.15}$. This result is very close to the result in Equation (8), which is unsurprising giving that we weight multiply observed sources as the reciprocal of the number of observations. Thus, it is difficult to tell if the degree to which Sgr A* is an outlier is a result of the relatively large intrinsic scatter or a result of substantially different accretion physics at low Eddington fractions. We also try fitting without Sgr A* represented at all, and the best-fit relation becomes

$$\mu = 0.49 \pm 0.23 + (1.05 \pm 0.11)R + (-0.50 \pm 0.19)X, \quad (10)$$

with an intrinsic scatter of $\ln \epsilon_\mu = -0.04_{-0.13}^{+0.15}$. Again, there is no significant difference with the result in Equation (8).

4.2. Radio-Active High/Soft State XRBs

The fundamental plane has generally been applied to low/hard state (and similar states) XRBs because in the high/soft states, jets are usually quenched (e.g., Tananbaum et al. 1972). In our XRB sample selection, however, we have taken an inclusive approach by including all detections that meet our criteria set forth in Section 2.2. This has resulted in two sources (4U 1543-47 and XTE J1550-564) with radio detections at nearly simultaneous epochs with X-ray spectra classifiable as very high or intermediate states. In both cases, the radio observations are less than 24 hr apart from the X-ray observations, and the radio emission is compact. As can be seen in Figures 6 and 7 the sources do not appear to be

substantial outliers compared to the other XRBs. Nevertheless, we may exclude them and Sgr A* from the sample, and the best-fit relation becomes

$$\mu = 0.51_{-0.24}^{+0.25} + (1.06_{-0.12}^{+0.11})R + (-0.51_{-0.18}^{+0.19})X, \quad (11)$$

with an intrinsic scatter of $\ln \epsilon_\mu = -0.02_{-0.13}^{+0.14}$. The small change from Equation (10) is likely a result of a combination of the fact that (i) only two sources have a single observation each in non-low/hard state and (ii) the radio-active intermediate- and high-state observations in our sample do not deviate strongly from low/hard state XRBs.

4.3. Optically Thick versus Optically Thin Radio Emission

We may expand on our examination of different states in XRBs by considering the influence of including AGNs with optically thin radio emission, which may arise from substantially older synchrotron emission than the currently observable X-ray emission. In all cases, we only use the compact, unresolved emission from any AGN, but with the exception of this subsection, we include the sources regardless of radio optical depth as determined by the spectral index. We use the radio spectral index of $\alpha = 0.4$ to delineate between optically thick $\alpha < 0.4$ and optically thin $\alpha \geq 0.4$ radio emission, recalling that we use the $S_\nu \propto \nu^{-\alpha}$ convention. The choice of $\alpha = 0.4$ as the division is conservative compared to more widely used value of 0.5, but makes no difference as there are no sources in our sample with radio spectra index in the range $0.35 < \alpha < 0.71$. As discussed in Section 3.1.3, some of our estimates of α come from two radio flux density measurements. The uncertainties in α (listed in Table 5) are generally small enough that we can determine whether a given source is flat or steep. There are, however, four sources with α estimates within 3σ of our flat/steep boundary (IC 4296, $\alpha = 0.1 \pm 0.24$; NGC 3607, $\alpha = 0.35 \pm 0.10$; NGC 5077, $\alpha = 0.32 \pm 0.07$; and NGC 5128, $\alpha = 0.33 \pm 0.06$). To account for these, we adopt the following method for estimating α from data for all AGNs. For each realization, we use flux densities sampled from the measurement with uncertainties assumed to be normally distributed with mean equal to the reported flux density and σ equal to the reported flux density uncertainty. Then, for each pair of flux density measurements, there is an implied $\alpha = \log(S_{\nu_1}/S_{\nu_2})/\log(\nu_2/\nu_1)$. For each realization, we treat the object according to the realized α as described below. Finally, we note that identifying objects as cores or jets based on measurements of α alone is still a heuristic as there are a non-negligible fraction of AGN cores identified at Very Long Baseline Array resolution that have $\alpha = 0.5$ –1.6 (Hovatta et al. 2014).

First, we remove all sources with $\alpha \geq 0.4$ as determined by the method described above. When doing so, our best fit is

$$\mu = 0.70_{-0.29}^{+0.28} + (1.10 \pm 0.12)R + (-0.53_{-0.21}^{+0.20})X, \quad (12)$$

with the natural logarithm of the intrinsic scatter $\ln \epsilon_\mu = 0.01_{-0.16}^{+0.17}$. This result is very close to our full sample results. Eight of the sources in our sample, however, do not have multi-frequency radio data sufficient for a robust measurement of α . In those cases, as described in Section 3.1.3, we have assumed an optically thick value $\alpha = 0 \pm 0.5$. If we remove those sources and only include AGNs with positive evidence for having a flat spectrum

($\alpha < 0.4$), the best-fit result is

$$\mu = 0.28_{-0.36}^{+0.32} + (0.92 \pm 0.15)R + (-0.18 \pm 0.29)X, \quad (13)$$

with the natural logarithm of the intrinsic scatter $\ln \epsilon_\mu = -0.04_{-0.21}^{+0.22}$. The difference between the above results and our full sample results is at slightly more than 1σ in the joint $\xi_{\mu R}$ – $\xi_{\mu X}$ posterior and is most likely a result of the decreased sample size when requiring positive evidence for optically thick radio emission. Our conclusion is that if the emission is sufficiently compact, as it is for our nearby sources at VLA resolution, then there is either unlikely to be substantial contamination from optically thin radio emission, or it makes little difference.

4.4. Seyferts on the Fundamental Plane

We consider whether Seyferts belong on the fundamental plane of black hole accretion. Some previous fundamental plane studies have restricted samples not to include Seyferts on the grounds that Seyferts are dominated by a radiatively efficient disk, which presumably will have a different correlation from low/hard state systems. In addition to this, at accretion rates high enough for an accreting black hole to be a Seyfert, the AGN should have quenched its jet and thus any radio emission seen is likely relic emission from an earlier epoch of low/hard state-like accretion. There are, however, Seyferts known to have compact flat or inverted-spectrum continuum radio emission at very long baseline interferometry resolution such as NGC 5033 (Giroletti & Panessa 2009). Thus, we have continued our empirical approach by including Seyferts as long as they met our criteria discussed in Section 2. It is, however, possible that at different accretion rates, different physics manifests itself in the radio and X-ray accretion. For this reason we try fitting the fundamental plane without Seyferts and only with Seyfert AGNs to see if any differences arise.

To cull Seyferts from our sample, we must first identify them. This work improves on our previous Seyfert identification method (Gültekin et al. 2009a), which relied solely on optical line ratios from Véron-Cetty & Véron (2006). The Véron-Cetty & Véron (2006) catalog and related material (e.g., Véron-Cetty & Véron 2010) is generally reliable for bright AGNs, but at low Eddington ratios the contamination from starlight in the host galaxies is substantial. This leads to, e.g., NGC 3607s being identified as a Seyfert despite the fact that (i) there is no obvious optical AGN and (ii) it has a 2–10 keV X-ray luminosity of $7.7 \times 10^{38} \text{ erg s}^{-2}$, corresponding to an X-ray Eddington fraction below 10^{-7} .

In this work we use the Ho et al. (1997) classification scheme if available for our sources and inspection of the X-ray spectrum if not. Ho et al. (1997) use information about the luminosity to inform whether to identify a source as a Seyfert. The approach of using the X-ray spectrum has the advantage of probing the bands more closely associated with the accretion inflow and jet production physics involved and allows one to inspect the data at hand to see if it is appropriate for inclusion. We classify objects as Seyferts if their X-ray spectrum requires a soft-excess component, a warm absorber, a Seyfert-like Fe line, or a pexmon reflection spectrum (Nandra et al. 2007). For nearly all cases where the source was in the Ho et al. (1997) catalog, our X-ray spectrum classification agreed. We identify Seyferts in Table 5.

When we remove Seyferts from our sample, the best-fit relation is

$$\mu = 0.53_{-0.23}^{+0.24} + (1.16 \pm 0.11)R + (-0.74_{-0.21}^{+0.20})X, \quad (14)$$

with an intrinsic scatter of $\ln \epsilon_\mu = -0.06_{-0.15}^{+0.16}$. This is very close to the results obtained from our full sample in Equation (8). Because this may be a result of the fact that there are relatively few Seyferts in our sample, we also fit to a sample in which the only AGN we include are Seyferts. In this case, the best-fit relation is

$$\mu = -1.15_{-0.60}^{+0.72} + (0.58_{-0.20}^{+0.24})R - (0.26_{-0.35}^{+0.30})X, \quad (15)$$

with an intrinsic scatter of $\ln \epsilon_\mu = -0.18_{-0.22}^{+0.26}$. Although the difference between this relation and the previous is large in absolute terms, it is still consistent at about the 2σ level in the joint posterior distribution of $\xi_{\mu R}$ and $\xi_{\mu X}$. The differences most likely show the result of having only seven Seyferts in our sample. Thus, we do not have sufficient data to state that radio-active Seyferts decidedly do or do not belong on the same fundamental plane relation.

4.5. Just AGN

In Gültekin et al. (2009a) we reported a difference between fundamental plane fits to an AGN-only sample and fits to samples with both AGNs and XRBs. Given the relatively few sources, it was not clear if AGNs and XRBs actually did not belong on the same relation or if small number statistics and the reduced dynamic range in mass can lead to fits of a 2D manifold in 3D space with an intrinsic scatter to a spurious result. Gültekin et al. (2014) tested for this by using some of the lowest-mass AGN available to put on the two different fundamental plane relations. These low-mass AGN were all Seyferts with masses determined from single-epoch $H\alpha$ line widths. We discussed above in Section 4.4 that we cannot definitively conclude that Seyferts belong on the same fundamental plane as the rest of the sample, but assuming that they do, the low-mass AGNs better followed the all black hole fundamental plane than the AGN-only fundamental plane. When limiting our current sample to only AGN, the best-fit relation is

$$\mu = 0.37 \pm 0.18 + (0.56_{-0.14}^{+0.13})R + (-0.29_{-0.13}^{+0.14})X, \quad (16)$$

with an intrinsic scatter of $\ln \epsilon_\mu = -0.30_{-0.15}^{+0.16}$. This is noticeably different from the fit in Equation (8) and very close to that found in Gültekin et al. (2009a). This reintroduces the possibility that there are real differences in the coupled radio and X-ray emission in AGNs and XRBs. Note that while the AGN-only fit parameters fall outside the 1σ intervals of the posterior probability distributions seen in Figure 5, the covariance between $\xi_{\mu R}$ and $\xi_{\mu X}$ does allow a decrease in $\xi_{\mu R}$ coupled with an increase in $\xi_{\mu X}$. Thus, the difference between the AGN-only fit and the full sample fit is at roughly the 2.4σ level. Given such a small difference, we cannot claim that the difference is significant as it is just as likely a result of the reduced dynamic range from limiting the sample to just AGNs. At 2.4σ , however, it is worth further investigation with a sample that expands the range of AGN masses.

4.6. Low Eddington Rates

A series of works (Li et al. 2008; Fan & Bai 2016; Xie & Yuan 2016, 2017; Qian et al. 2017) suggests that at the lowest accretion rates, the fundamental plane will take a different form. To investigate this, we restrict our sample to only sources with $L_X/L_{\text{Edd}} < 10^{-6}$. This has the effect of limiting the sample to only AGNs (see Figure 2) so that the issues raised in Section 4.5 apply here as well. The best-fit relation is

$$\mu = 0.69 \pm 0.18 + (0.35_{-0.16}^{+0.17})R + (0.06_{-0.22}^{+0.21})X, \quad (17)$$

with an intrinsic scatter of $\ln \epsilon_\mu = -0.67_{-0.21}^{+0.23}$. Here we note that Sgr A* may have a substantial influence on the overall fit. If we also exclude Sgr A* from the sample, the best fit is

$$\mu = 0.74_{-0.21}^{+0.20} + (0.29 \pm 0.20)R + (0.21_{-0.34}^{+0.33})X, \quad (18)$$

with an intrinsic scatter of $\ln \epsilon_\mu = -0.67 \pm 0.25$. The difference in results between Equations (17) and (18) is not significant.

4.7. Regression in Other Directions

Because the focus of this work is to provide a mass estimator, we have until now only done a regression analysis with R and X as the independent variables. This results in a mean value of μ for given values of R and X . Inverting the best-fit plane found in this method to predict R or X from two other measurements, however, is not appropriate. In this section, we report results from regression with R or X as the dependent variable. In the case of using radio as the dependent variable, the best-fit relation is

$$R = -0.62_{-0.17}^{+0.15} + (0.70_{-0.09}^{+0.08})X + (0.74 \pm 0.06)\mu, \quad (19)$$

with an intrinsic scatter in the log-radio direction of $\ln \epsilon_R = -0.23_{-0.13}^{+0.14}$. In the case of using X-ray as the dependent variable, the best-fit relation is

$$X = 0.58 \pm 0.23 + (-0.59 \pm 0.15)\mu + (0.99_{-0.13}^{0.12})R, \quad (20)$$

with an intrinsic scatter in the log-X-ray direction of $\ln \epsilon_X = -0.03_{-0.14}^{+0.15}$. The intrinsic scatters measured by regressing in the log-radio and log-X-ray directions are not significantly smaller, though there is a suggestion that it is smaller in the R direction.

4.8. Summary of Differences between Current Work and Gültekin et al. (2009a)

As this work is an extension of the work started by Gültekin et al. (2009a), it is worth directly comparing and contrasting the work done here with the earlier work in terms of data, analysis, and conclusions. In this subsection we summarize the advances made in this work. First, and most importantly, we have increased the sample size of AGNs with primary direct mass measurements and requisite radio and X-ray data from 18 to 30, roughly doubling (Section 2.1). Second, we have improved our selection of XRBs so that our analysis is not hindered by poor distance or mass estimates (Section 2.2). Third, we improved our identification and handling of Seyferts (Section 4.4). Fourth, we have improved our analysis so that we now (i) include a treatment of correlated uncertainties (Section 3.1), (ii) handle multiple observations of individual objects to increase

the information available (Section 3.1.8), (iii) have an improved handling of contamination of AGN X-ray flux measurements from background AGN (Section 3.1.5) and XRBs near the galaxy center (Section 3.1.6), (iv) statistically treat the effects of non-simultaneous observations of X-ray and radio fluxes, and (iv) use MCMC methods (Section 3.2) rather than a merit function, which has some disadvantages (Plotkin et al. 2012).

The above improvements in data selection and analysis have allowed us to better consider two speculations raised in Gültekin et al. (2009a). First, Gültekin et al. (2009a) compared fits to two subsamples of the earlier, smaller parent sample: one subsample whose AGN consisted only of LLAGN and LINERs and another subsample whose AGN consisted only of Seyferts. In doing so, they Gültekin et al. (2009a) found a much smaller intrinsic scatter in the LLAGN/LINER subsample as well as a statistically different fit. As mentioned above, we now have a larger sample and an improved identification of Seyferts. With the improved sample and identification, we no longer find a significant difference in the intrinsic scatter, nor in the fundamental plane fit parameters (Section 4.4). Second, Gültekin et al. (2009a) compared an AGN-only sample to a sample with both XRBs and AGNs. In the comparing these two samples, Gültekin et al. (2009a) found a significant difference between the fits, suggesting the possibility that the fundamental plane was not fundamental to all black holes but that there were separate relations for XRBs and AGNs. Based on our improved sample and in combination with results of Gültekin et al. (2014), we no longer have strong evidence supporting this speculation, though it is worth testing with as large a dynamic range in AGN mass as possible (Section 4.5).

Finally, a major goal of this project is to give the best possible mass estimation tool. The mass-predictor relation we present in this work (given the discussion below in Section 5) is more robust than the relation presented by Gültekin et al. (2009a). The robustness comes from all of the above-mentioned improvements in data and analysis.

As an example of the significant improvements made in this paper, we consider how the mass estimation tool we present in this paper better predicts the mass of the black holes in M87 and GRS 1915+104. The black hole in M87 has logarithmic mass in solar units of $\mu = 9.79 \pm 0.03$ (Gebhardt et al. 2011, but see also Walsh et al. 2013). Based on the data provided in Table 5, our current mass estimator based on the fundamental plane of black hole accretion is $\mu = 10.14 \pm 0.96$, well within the measured scatter of the relation. On the other hand, the mass predicted by Equation (6) in Gültekin et al. (2009a) is $\mu 8.90 \pm 0.77$. The discrepancy is even more apparent at the low-mass end, such as for GRS 1915+104, which would be predicted to have a logarithmic mass of $\mu = 2.2 \pm 0.96$ with our current relation but a mass of $\mu = 5.4 \pm 0.96$ with the older version. Thus, with the current relation, one would correctly identify it as consistent with a stellar mass black hole, while with the old relation one would conclude that it is either an IMBH or a low-mass AGN. The underlying reason for this is that the mass-predictor regressions in Gültekin et al. (2009a) only used AGN sources as they were only intended to be used for AGNs. With the currently better measured intrinsic scatter of $\ln \epsilon_0 = -0.04$, it is clear that one of the best uses for this mass-predictor relation is for discerning between XRBs, IMBHs, and AGNs, and this requires a mass-predictor relation that uses XRB data as we have done here. We also reported

regressions for the prediction of radio luminosity in Equation (19) and of X-ray luminosity in Equation (20), the latter of which has not been reported in the literature before.

4.9. Future Work

We finally note that we expect that further improvements of the fundamental plane can be made by including more XRBs and expanding the mass range of AGNs in the sample. The mass range of AGNs in the sample can be improved by targeting known high-mass AGNs with current instrumentation as well as future instrumentation. In particular, high-mass AGNs are difficult to measure black hole masses because of (i) their typical distances, which can be addressed with Atacama Large Millimeter Array and 30 m class infrared telescopes with adaptive optics and/or (ii) their low surface brightnesses, which can be addressed with 30 m class telescopes and the *James Webb Space Telescope*. With more high-mass AGNs, the lever arm of the fits will be better established. Low-mass AGNs also require high-angular resolution instrumentation in optical or infrared to measure black hole masses as well as sensitive and high-angular X-ray and radio instruments, e.g., Lynx (Gaskin et al. 2017) and Next Generation VLA (Carilli et al. 2015), to probe the typically fainter sources and rule out contamination from XRBs.

5. How to Estimate Black Hole Masses with the Fundamental Plane

For those who wish to use the fundamental plane of black hole accretion to estimate the mass of a black hole, we provide the following guidelines. First, the prospective mass estimator needs some assurances that the object in question is a black hole or should explicitly acknowledge that they are making such an assumption. The fundamental plane we have studied here only uses known black holes—at least to the extent that any given XRB or AGN is known to be a black hole. The fundamental plane does not, by itself, constitute a means for discriminating between black holes and other objects, though other means for such an exercise exist (Strader et al. 2012).

Second, mass estimation from the $M-L_R-L_X$ relation requires good L_R and L_X data. Because we do not use upper limits in our analysis, the data must be detections in both cases. The best data will have high-angular resolution to avoid contamination from other sources of radio or X-ray emission. This is especially important at low X-ray luminosities of AGNs, which could be confused with XRBs. Radio data should be converted to 5 GHz in a manner similar to the one described in Section 3.1.3 and to use 2–10 keV power-law continuum flux. Obviously, one needs the distance to turn what assumes and hopes is isotropic flux into a luminosity. The radio and X-ray data ought to be from a similar epoch, the closer in time the better. As a very rough rule of thumb, we recommend they be observed within $\Delta t < (2+M/10^6 M_\odot)$ day. Obviously, without knowing the mass of the black hole one is trying to estimate, it is impossible to know how close to simultaneous one must schedule the observations, but one may see what masses they are sensitive to.

Finally, recognize that there is substantial intrinsic scatter in the relation of an assumed normal distribution with $\epsilon_\mu = 1$ dex. This means, for example, that for a large collection of black holes with masses estimated from the fundamental plane to be $10^8 M_\odot$, 5% of them will be below $10^6 M_\odot$ or above $10^{10} M_\odot$,

assuming that all logarithmic black hole masses are equally represented. This makes it a relatively crude tool for black hole-mass estimation, but if it is the only tool available, it will be the best tool available.

The fundamental plane is most useful in mass estimation when one wants to discriminate between an XRB and an IMBH or AGN. The fundamental plane is also useful in estimating the mass of a Type 2 AGN (without broad lines) in a galaxy without a well-defined bulge from which to use host-galaxy scaling relations.

Given the above considerations, then we recommend the use of the following mass estimator:

$$\mu = 0.55 \pm 0.22 + (1.09 \pm 0.10)R + (-0.59^{+0.16}_{-0.15})X. \quad (21)$$

One source of data for which the fundamental plane could prove especially useful is that from extended Roentgen Survey with an Imaging Telescope Array (eROSITA) on the Spectrum-Röntgen-Gamma satellite (Predehl et al. 2010; Merloni et al. 2012). Expected to detect $\sim 3 \times 10^6$ AGNs in the 2–10 keV band, eROSITA will provide half of the needed data to use the fundamental plane for black hole-mass estimation. A radio survey of the detected AGNs would complete the necessary data to make a black hole-mass catalog.

6. Summary

In this paper we have analyzed the dependence of an accreting black hole’s mass on its radio and X-ray emission. Using only black holes with high-quality, direct, primary mass measurements and sensitive, high-spatial-resolution radio and X-ray data, we used MCMC methods to find the best mass-predictor relation to be

$$\mu = 0.55 \pm 0.22 + (1.09 \pm 0.10)R + (-0.59^{+0.16}_{-0.15})X \quad (22)$$

with the natural logarithm of the intrinsic scatter $\ln \epsilon_\mu = -0.04^{+0.14}_{-0.13}$. After considering a number of potential modifications to our original, inclusive sample, we conclude that the fundamental plane can be used to describe any accreting black hole with both X-ray and compact radio emission. In particular, we cannot rule out that radio-active high/soft state XRBs and radio-active Seyferts are inconsistent with the fundamental plane made up of low/hard state XRBs and LLAGNs and LINERs. The low numbers of radio-active high/soft state XRBs and radio-active Seyferts, however, make such conclusions tentative and warrant further study. Given the wide variety of sources that are included in our sample and the substantial intrinsic scatter we found, the fundamental plane is a useful—though relatively low precision—tool for estimating black hole masses.

K.G. acknowledges support provided by NASA through *Chandra* Award Number GO0-11151X issued by the *Chandra* X-ray Observatory Center, which is operated by the Smithsonian Astrophysical Observatory for and on behalf of NASA under contract NAS8-03060. K.G. acknowledges support provided by the Fund for Astrophysics Research. A.L.K. would like to thank the support provided by NASA through Einstein Postdoctoral Fellowship Grant No. PF4-150125 awarded by the *Chandra* X-ray Center, operated by the Smithsonian Astrophysical Observatory for NASA under contract NAS8-03060

The National Radio Astronomy Observatory is a facility of the National Science Foundation operated under cooperative agreement by Associated Universities, Inc.

This research has made use of the NASA/IPAC Extragalactic Database, which is operated by the Jet Propulsion Laboratory, California Institute of Technology, under contract with the National Aeronautics and Space Administration. This research has made use of NASA’s Astrophysics Data System.

Appendix A New Radio Data

We obtained new VLA observations of the nuclei of 12 galaxies harboring massive black holes with direct dynamical mass measurement (Project ID SB0514). Our observations were centered at 8.46 GHz with a total bandwidth of 256 MHz while the array was in its most extended A configuration, leading to a typical angular resolution of $0''.3$. With a total time of 60 minutes for each source, the time-on-source integration varied but ranged from 25–33 minutes for theoretical sensitivities in the range $15\text{--}22 \mu\text{Jy beam}^{-1}$. Each scheduling block began with scans of the corresponding flux calibrator source given in Table 1 to set the flux density scale to an accuracy of 5% and calibrate the bandpass (Perley & Butler 2013). We performed phase-referencing using a nearby complex gain calibrator within 10 degrees. Standard VLA calibration and imaging procedures were followed using CASA version 5.3.0.

After inspecting for radio frequency interference, data were averaged in 30 s temporal bins and 8- or 10-channel frequency bins. We made images and processed with the CLEAN algorithm for imaging. For CLEAN we halted processing at a value of 2.5 times the dirty map rms, which was typically very close to the theoretical noise, using a gain of 0.1 and robust weighting with a robust parameter of 0.5. Our images (Figure 8) used a cell size of $0''.05$ with a total image size of 8192×8192 , compared to our field of view of $5''.3$. For NGC 4486A we used an image size of 32768×32768 in order to avoid side lobes coming from NGC 4486, but in the end we were unable to detect emission from NGC 4486A. For the choices above, we tried several different variations but found that it made very little difference.

For each of the processed images, we looked for emission at the location of the galaxy nucleus. Of the 12 galaxies, 6 had unambiguous point sources at the expected location. For the detections, we found that the radio flux was spatially coincident with the X-ray point source found. We attribute all of this emission to the central black hole. We calculated the flux density from these sources by fitting a two-dimensional elliptical Gaussian to the point source in a 20×20 pixel region and use the total flux returned by the CASA imfit tool. We list in Table 1 flux densities and their uncertainties, calculated as the quadrature sum of fit uncertainty, image rms noise, and a 3% uncertainty for absolute flux calibration (Perley & Butler 2013). Undetected sources are reported as upper limits at 3 times the flux uncertainty.

Appendix B Archival Radio Data

In addition to our new radio data, we also analyzed 21 archival VLA radio data sets. Some of the data in this had been previously published but had concentrated on radio emission

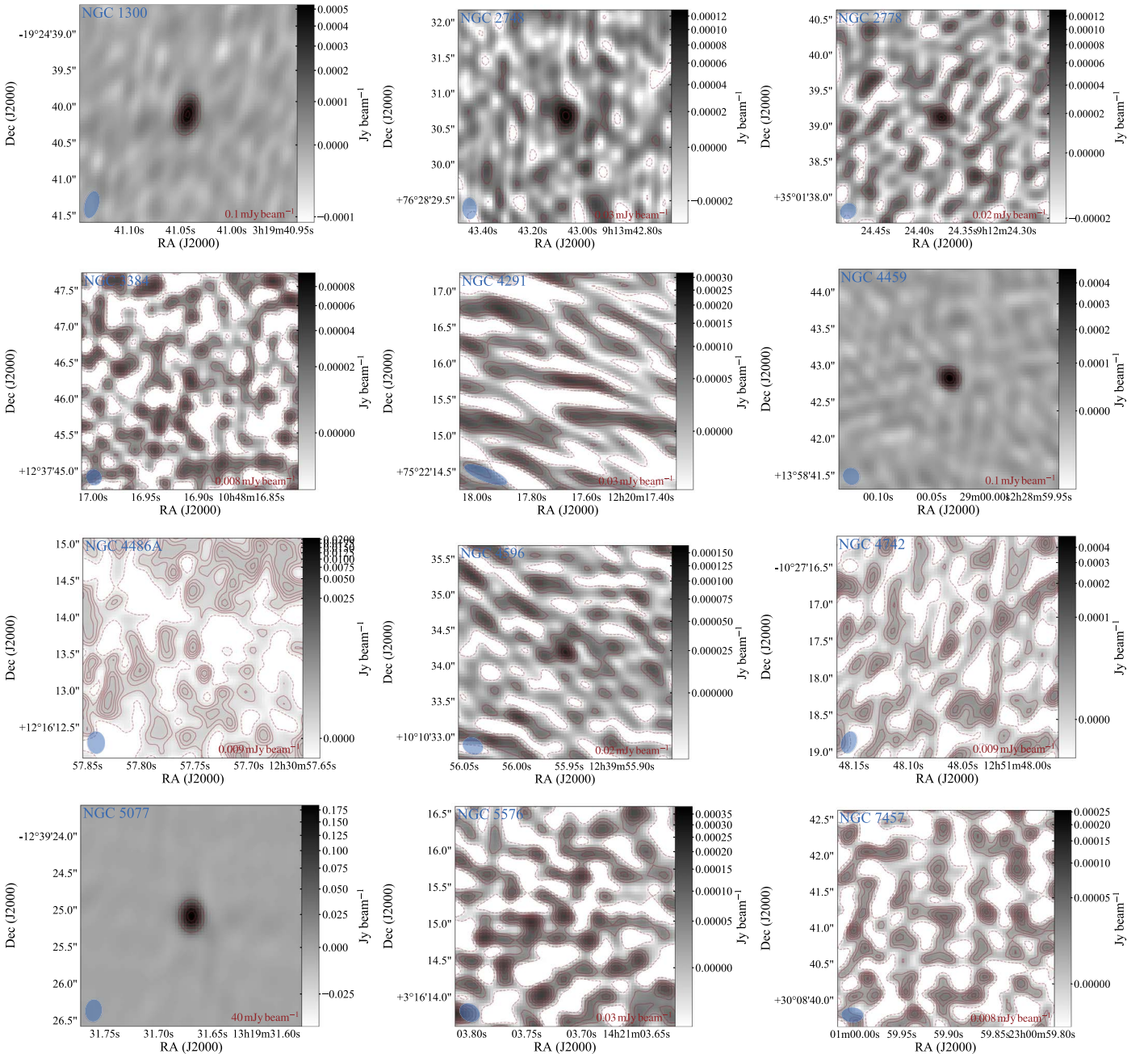


Figure 8. VLA maps of our new 8.4 GHz X-band observations of 12 sources. Grayscale is indicated by the bar to the right of each panel, and the contours are in constant steps of the value indicated in the lower-right corner of each panel. The blue ellipse in the lower-right corner of each panel shows the size and position angle of the synthesized beam. The maps are centered on the brightest pixel within a 20×20 pixel region centered on the Simbad coordinates for the host galaxy. When the source is securely detected, it is always consistent with a point source. We list the integrated flux densities and upper limits in Table 1.

that was not continuum core emission. We analyzed these data sets in the same way as outlined in Appendix A, and we present the results in Table 2.

Appendix C Archival X-Ray Data

The X-ray data for our AGN sample consists of our archival X-ray analysis in Gültekin et al. (2009a), analysis of new *Chandra* data in Gültekin et al. (2012), and a separate analysis of archival data in this work, including analysis of archival data of NGC 4486 at two epochs, which we average into a single

X-ray flux for our fundamental plane analysis. In this appendix we describe this most recent archival data analysis.

We use the same method of analysis as in Gültekin et al. (2009a, 2012), both of which can be consulted for further details but which we summarize here. All data reduction was performed with CIAO version 4.y and calibration database (CALDB) version 4.6.7 using newly created level 2 event files. Source identification was done with a combination of wavdetect and manual inspection of each *Chandra* image. Some sources, especially those in central early-type galaxies, did not register as a point source with wavdetect because of being surrounded by diffuse X-ray emission, presumably from

hot gas. For such sources where any AGN emission was dominated by surrounding hot gas emission, the best that could be done was to estimate an upper limit on the flux by performing a background subtraction under the assumption that there was a point source at the center. This upper limit to nuclear flux is a combination of AGN and XRBs, but it does not affect the rest of our analysis in the paper. All source locations were compared with optical and near-infrared images of the host galaxy to ensure that we were selecting the likely central X-ray source. In cases where there were multiple X-ray point sources consistent with the optical/near-infrared center of the galaxy, we registered the *Chandra* image with the Sloan Digital Sky Survey or Deep Near Infrared Survey coordinates as best possible using common background AGNs. We then took the source closest to the peak of the galaxy starlight. Background regions were selected using an annulus with inner radius equal to the source region radius of between 1.5 and 3", depending on potential contamination from surrounding X-ray emission. The outer radius of the background annulus was chosen to include sufficient counts to generate a background. We used the *specextract* tool provided by CIAO to extract spectra and to create auxiliary response files and response matrix files for the source and background spectra.

Spectral fitting was done with XSPEC version 12 (Arnaud 1996). All spectra were fit with a photoabsorbed power law with N_H column density set to the Galactic value toward the source Kalberla et al. (2005). For the sources that had sufficient counts to warrant more detailed fitting, we also included a redshifted intrinsic photoabsorption component with a column density that was allowed to vary. When required by the spectra, we also included other components to fully explain the data, especially APEC, pexmon, and blackbody models to account for soft emission and Gaussian features to account for emission lines. In the vast majority of cases, the inclusion of the softer components did not make more than a 2σ difference in the 2–10 keV power-law flux. If we were unable to rule out zero flux from a power-law in the 2–10 keV band at the 3σ level, we considered it an upper limit. We report the results of our X-ray spectral fits in Table 3.

Appendix D XRB Data

We list our sample of XRBs with distances and masses in Table 4. A recent examination of *Gaia* data has new distance estimates for 4 of our 6 XRBs (Gandhi et al. 2018). Of those 4, three of the distance estimates are based on *Gaia* measurements with goodness of fit metrics greater than +3, which indicates a bad astrometric fit. The final source, 4U 1543-47, for which we use distance of 7.5 ± 1 kpc due to Park et al. (2004), has new distance estimates of 24.72 ± 41.15 , $7.02^{+2.85}_{-1.86}$, and $10.11^{+4.33}_{-3.53}$ kpc, depending on the Bayesian priors assumed. Given the order of magnitude range in distances acceptable for this source, it is not clear that it is an improvement on our adopted distance. Nevertheless, we ran our analysis using distances for all four sources from Gandhi et al. (2018) based on their “ r_{exp} prior.” The quantitative differences in the fit results for the full sample were less than 1% of the 68% uncertainty range, indicating no difference to the results of this paper.

Our data for XRBs consists of literature radio data and a combination of literature X-ray data and our analysis of

archival *RXTE* data for sources 4U 1543-47, GRO J1655-40, XTE J1118+480, and XTE J15550-564.

X-ray spectral fitting to 4U 1543-47 for observation on MJD = 52490.14009 was done using a photoabsorbed power-law model (`phabs(pow)`) with an absorption column fixed to $N_H = 4.0 \times 10^{21} \text{ cm}^{-2}$. Our spectral fitting yielded a constraint on the power-law component’s photon index of $\Gamma = 1.82 \pm 0.03$. For the observation on MJD = 52445.60917, during which 4U 1543-47 was in a very high state, we used a photoabsorbed accretion-disk emission-line plus accretion-disk blackbody plus power-law model (`phabs(laor + bbody + pow)`) with an absorption column fixed to $N_H = 4.0 \times 10^{21} \text{ cm}^{-2}$. The power-law photon index was constrained to $\Gamma = 2.51 \pm 0.01$.




X-ray spectral fitting to GRO J1655-40 was done using a model of a photoabsorbed accretion-disk emission-line plus power-law model (`phabs(laor + pow)`) with an absorption column fixed to $N_H = 9.0 \times 10^{21} \text{ cm}^{-2}$. The power-law varied slightly among the four observations from $\Gamma = 1.32 \pm 0.02$ to 1.47 ± 0.01 .

X-ray spectral fitting to XTE J1118+480 was done using an absorbed power-law model in the 3–25 keV range using standard data products in the archive. We added 0.6% systematic errors to all channels, and adopted an absorption column of $N_H = 1.4 \times 10^{20} \text{ cm}^{-2}$ with Tuebingen-Boulder interstellar medium absorption model (`tbabs`). For all observations, the power-law photon index changed very little, from $\Gamma = 1.715 \pm 0.004$ to 1.721 ± 0.004 .

X-ray spectral fitting to XTE J15550-564 for the observation on MJD = 51664.42194, during which it was in a very high state, was done using a photoabsorbed accretion-disk emission-line plus accretion-disk blackbody plus power-law model (`phabs(laor + bbody + pow)`) with an absorption column fixed to $N_H = 9.0 \times 10^{21} \text{ cm}^{-2}$. The fit constrained the power-law photon index to be $\Gamma = 2.22 \pm 0.01$. The observation on MJD = 51696.48361, during which the source was in a low/hard state, was fitted with a photoabsorbed power-law model (`phabs(pow)`) with the same fixed absorption column. The photon index was constrained to be $\Gamma = 1.64 \pm 0.01$.

We list the radio and X-ray observational data in Table 6.

ORCID iDs

Kayhan Gültekin  <https://orcid.org/0000-0002-1146-0198>
Edward M. Cackett  <https://orcid.org/0000-0002-8294-9281>
Sera Markoff  <https://orcid.org/0000-0001-9564-0876>

References

- Arnaud, K. A. 1996, in ASP Conf. Ser. 101, *Astronomical Data Analysis Software and Systems V*, ed. G. H. Jacoby & J. Barnes (San Francisco, CA: ASP), 17
- Atkinson, J. W., Collett, J. L., Marconi, A., et al. 2005, *MNRAS*, 359, 504
- Baganoff, F. K., Bautz, M. W., Brandt, W. N., et al. 2001, *Natur*, 413, 45
- Barth, A. J., Sarzi, M., Rix, H.-W., et al. 2001, *ApJ*, 555, 685
- Barthelmy, S. D., D’Ai, A., D’Avanzo, P., et al. 2015, *GCN*, 17929, 1
- Bauer, F. E., Alexander, D. M., Brandt, W. N., et al. 2004, *AJ*, 128, 2048
- Beck, R., Shoutenkov, V., Ehle, M., et al. 2002, *A&A*, 391, 83
- Bender, R., Kormendy, J., Bower, G., et al. 2005, *ApJ*, 631, 280
- Blandford, R. D., & McKee, C. F. 1982, *ApJ*, 255, 419
- Boroson, T. A. 2002, *ApJ*, 565, 78
- Boroson, T. A., & Green, R. F. 1992, *ApJS*, 80, 109
- Bower, G. A., Green, R. F., Bender, R., et al. 2001, *ApJ*, 550, 75
- Brandt, W. N., & Hasinger, G. 2005, *ARA&A*, 43, 827
- Brandt, W. N., Hornschemeier, A. E., Alexander, D. M., et al. 2001, *AJ*, 122, 1

- Capetti, A., Kharb, P., Axon, D. J., Merritt, D., & Baldi, R. D. 2009, *AJ*, **138**, 1990
- Cappellari, M., Neumayer, N., Reunanen, J., et al. 2009, *MNRAS*, **394**, 660
- Cappellari, M., Verolme, E. K., van der Marel, R. P., et al. 2002, *ApJ*, **578**, 787
- Carilli, C. L., McKinnon, M., Ott, J., et al. 2015, arXiv:1510.06438
- Coccatto, L., Sarzi, M., Pizzella, A., et al. 2006, *MNRAS*, **366**, 1050
- Condon, J. J., Cotton, W. D., Greisen, E. W., et al. 1998, *AJ*, **115**, 1693
- Corbel, S., Kaaret, P., Jain, R. K., et al. 2001, *ApJ*, **554**, 43
- Cowie, L. L., Garmire, G. P., Bautz, M. W., et al. 2002, *ApJL*, **566**, L5
- Cretton, N., & van den Bosch, F. C. 1999, *ApJ*, **514**, 704
- Dalla Bontà, E., Ferrarese, L., Corsini, E. M., et al. 2009, *ApJ*, **690**, 537
- Davies, R. I., Thomas, J., Genzel, R., et al. 2006, *ApJ*, **646**, 754
- Davis, T. A., Bureau, M., Cappellari, M., Sarzi, M., & Blitz, L. 2013, *Natur*, **494**, 328
- de Francesco, G., Capetti, A., & Marconi, A. 2008, *A&A*, **479**, 355
- Dhawan, V., Pooley, G. G., Ogley, R. N., & Mirabel, I. F. 2000, *IAU Circ.*, **7395**
- Doeleman, S. S., Weintraub, J., Rogers, A. E. E., et al. 2008, *Natur*, **455**, 78
- Dong, A.-J., Wu, Q., & Cao, X.-F. 2014, *ApJL*, **787**, L20
- Dressel, L. L., & Condon, J. J. 1978, *ApJS*, **36**, 53
- Elmouttie, M., Haynes, R. F., Jones, K. L., et al. 1997, *MNRAS*, **284**, 830
- Emsellem, E., Dejonghe, H., & Bacon, R. 1999, *MNRAS*, **303**, 495
- Evans, D. A., Hardcastle, M. J., Croston, J. H., Worrall, D. M., & Birkinshaw, M. 2005, *MNRAS*, **359**, 363
- Fabbiano, G., Gioia, I. M., & Trinchieri, G. 1989, *ApJ*, **347**, 127
- Falcke, H., Körding, E., & Markoff, S. 2004, *A&A*, **414**, 895
- Fan, X.-L., & Bai, J.-M. 2016, *ApJ*, **818**, 185
- Fender, R. P., Hjellming, R. M., Tilanus, R. P. J., et al. 2001, *MNRAS*, **322**, L23
- Ferrarese, L., & Ford, H. C. 1999, *ApJ*, **515**, 583
- Ferrarese, L., Ford, H. C., & Jaffe, W. 1996, *ApJ*, **470**, 444
- Filho, M. E., Barthel, P. D., & Ho, L. C. 2006, *A&A*, **451**, 71
- Filho, M. E., Fraternali, F., Markoff, S., et al. 2004, *A&A*, **418**, 429
- Foreman-Mackey, D. 2016, *JOSS*, **1**, 24
- Gallimore, J. F., Axon, D. J., O'Dea, C. P., Baum, S. A., & Pedlar, A. 2006, *AJ*, **132**, 546
- Gallo, E., Fender, R. P., & Pooley, G. G. 2003, *MNRAS*, **344**, 60
- Gallo, E., Miller, B. P., & Fender, R. 2012, *MNRAS*, **423**, 590
- Gandhi, P., Rao, A., Johnson, M. A. C., Paice, J. A., & Maccarone, T. J. 2018, arXiv:1804.11349
- Gaskin, J. A., Allured, R., Bandler, S. R., et al. 2017, *Proc. SPIE*, **10397**, 103970S
- Gebhardt, K., Adams, J., Richstone, D., et al. 2011, *ApJ*, **729**, 119
- Gebhardt, K., Lauer, T. R., Kormendy, J., et al. 2001, *AJ*, **122**, 2469
- Gebhardt, K., Lauer, T. R., Pinkney, J., et al. 2007, *ApJ*, **671**, 1321
- Genzel, R., Eisenhauer, F., & Gillessen, S. 2010, *RvMP*, **82**, 3121
- Giroletti, M., & Panessa, F. 2009, *ApJL*, **706**, L260
- Goodman, J., & Weare, J. 2010, *Communications in Applied Mathematics and Computational Science*, **5**, 65
- Greene, J., Bailyn, C. D., & Orosz, J. A. 2001, *ApJ*, **554**, 1290
- Greenhill, L. J., Booth, R. S., Ellingsen, S. P., et al. 2003, *ApJ*, **590**, 162
- Greenhill, L. J., Moran, J. M., & Herrnstein, J. R. 1997, *ApJL*, **481**, L23
- Grimm, H.-J., Gilfanov, M., & Sunyaev, R. 2003, *MNRAS*, **339**, 793
- Gültekin, K., Cackett, E. M., King, A. L., Miller, J. M., & Pinkney, J. 2014, *ApJL*, **788**, L22
- Gültekin, K., Cackett, E. M., Miller, J. M., et al. 2009a, *ApJ*, **706**, 404
- Gültekin, K., Cackett, E. M., Miller, J. M., et al. 2012, *ApJ*, **749**, 129
- Gültekin, K., Richstone, D. O., Gebhardt, K., et al. 2009b, *ApJ*, **695**, 1577
- Gültekin, K., Richstone, D. O., Gebhardt, K., et al. 2009c, *ApJ*, **698**, 198
- Gültekin, K., Richstone, D. O., Gebhardt, K., et al. 2011, *ApJ*, **741**, 38
- Hannikainen, D. C., Hunstead, R. W., Campbell-Wilson, D., & Sood, R. K. 1998, *A&A*, **337**, 460
- Hasinger, G., Altieri, B., Arnaud, M., et al. 2001, *A&A*, **365**, L45
- Healey, S. E., Romani, R. W., Taylor, G. B., et al. 2007, *ApJS*, **171**, 61
- Heckman, T. M., Crane, P. C., & Balick, B. 1980, *A&AS*, **40**, 295
- Heinz, S. 2004, *MNRAS*, **355**, 835
- Heinz, S., & Sunyaev, R. A. 2003, *MNRAS*, **343**, L59
- Hirabayashi, H., Fomalont, E. B., Horiuchi, S., et al. 2000, *PASJ*, **52**, 997
- Ho, L. C., Filippenko, A. V., & Sargent, W. L. W. 1997, *ApJ*, **487**, 568
- Ho, L. C., & Ulvestad, J. S. 2001, *ApJS*, **133**, 77
- Houghton, R. C. W., Magorrian, J., Sarzi, M., et al. 2006, *MNRAS*, **367**, 2
- Hovatta, T., Aller, M. F., Aller, H. D., et al. 2014, *AJ*, **147**, 143
- Huré, J.-M. 2002, *A&A*, **395**, L21
- Huré, J.-M., Hersant, F., Surville, C., Nakai, N., & Jacq, T. 2011, *A&A*, **530**, A145
- Israel, F. P., Mahoney, M. J., & Howarth, N. 1992, *A&A*, **261**, 47
- Jardel, J. R., Gebhardt, K., Shen, J., et al. 2011, *ApJ*, **739**, 21
- Jones, D. L., & Wehrle, A. E. 1997, *ApJ*, **484**, 186
- Jonker, P. G., & Nelemans, G. 2004, *MNRAS*, **354**, 355
- Kalberla, P. M. W., Burton, W. B., Hartmann, D., et al. 2005, *A&A*, **440**, 775
- Kalemci, E., Tomsick, J. A., Buxton, M. M., et al. 2005, *ApJ*, **622**, 508
- Kim, D.-W., & Fabbiano, G. 2004, *ApJ*, **611**, 846
- King, A. L., Miller, J. M., Raymond, J., Reynolds, M. T., & Morningstar, W. 2015, *ApJL*, **813**, L37
- Kondratko, P. T., Greenhill, L. J., & Moran, J. M. 2008, *ApJ*, **678**, 87
- Kormendy, J., Bender, R., Magorrian, J., et al. 1997, *ApJL*, **482**, L139
- Kormendy, J., & Ho, L. C. 2013, *ARA&A*, **51**, 511
- Krajnović, D., McDermid, R. M., Cappellari, M., & Davies, R. L. 2009, *MNRAS*, **399**, 1839
- Kuo, C. Y., Braatz, J. A., Condon, J. J., et al. 2011, *ApJ*, **727**, 20
- Kuulkers, E., Motta, S., Kajava, J., et al. 2015, *ATel*, **7647**, 1
- Laurent-Muehleisen, S. A., Kollgaard, R. I., Ryan, P. J., et al. 1997, arXiv:astro-ph/9607058
- Li, Z.-Y., Wu, X.-B., & Wang, R. 2008, *ApJ*, **688**, 826
- Liuzzo, E., Giovannini, G., Giroletti, M., & Taylor, G. B. 2010, *A&A*, **516**, A1
- Lodato, G., & Bertin, G. 2003, *A&A*, **398**, 517
- Marconi, A., Axon, D. J., Capetti, A., et al. 2003, *ApJ*, **586**, 868
- Markoff, S., Nowak, M., Corbel, S., Fender, R., & Falcke, H. 2003, *A&A*, **397**, 645
- McClintock, J. E., Garcia, M. R., Caldwell, N., et al. 2001, *ApJL*, **551**, L147
- McConnell, N. J., Ma, C.-P., Graham, J. R., et al. 2011, *ApJ*, **728**, 100
- McConnell, N. J., Ma, C.-P., Murphy, J. D., et al. 2012, *ApJ*, **756**, 179
- Merloni, A., Heinz, S., & Di Matteo, T. 2003, *MNRAS*, **345**, 1057
- Merloni, A., Körding, E., Heinz, S., et al. 2006, *NewA*, **11**, 567
- Merloni, A., Predehl, P., Becker, W., et al. 2012, arXiv:1209.3114
- Merritt, D., Ferrarese, L., & Joseph, C. L. 2001, *Sci*, **293**, 1116
- Miller, J. M., & Gültekin, K. 2011, *ApJL*, **738**, L13
- Miller, J. M., Pooley, G. G., Fabian, A. C., et al. 2012, *ApJ*, **757**, 11
- Moretti, A., Campana, S., Lazzati, D., & Tagliaferri, G. 2003, *ApJ*, **588**, 696
- Morganti, R., Tsvetanov, Z. I., Gallimore, J., & Allen, M. G. 1999, *A&AS*, **137**, 457
- Müller, C., Kadler, M., Ojha, R., et al. 2011, *A&A*, **530**, L11
- Muno, M. P., Remillard, R. A., Morgan, E. H., et al. 2001, *ApJ*, **556**, 515
- Murphy, T., Sadler, E. M., Ekers, R. D., et al. 2010, *MNRAS*, **402**, 2403
- Nagar, N. M., Falcke, H., & Wilson, A. S. 2005, *A&A*, **435**, 521
- Nagar, N. M., Falcke, H., Wilson, A. S., & Ulvestad, J. S. 2002, *A&A*, **392**, 53
- Nagar, N. M., Wilson, A. S., & Falcke, H. 2001, *ApJL*, **559**, L87
- Nandra, K., O'Neill, P. M., George, I. M., & Reeves, J. N. 2007, *MNRAS*, **382**, 194
- Nowak, M. A., Neilsen, J., Markoff, S. B., et al. 2012, *ApJ*, **759**, 95
- Nowak, N., Saglia, R. P., Thomas, J., et al. 2007, *MNRAS*, **379**, 909
- Nowak, N., Saglia, R. P., Thomas, J., et al. 2008, *MNRAS*, **391**, 1629
- Nowak, N., Thomas, J., Erwin, P., et al. 2010, *MNRAS*, **403**, 646
- Nyland, K., Young, L. M., Wrobel, J. M., et al. 2016, *MNRAS*, **458**, 2221
- Orosz, J. A. 2003, in *IAU Symp. 212, A Massive Star Odyssey: From Main Sequence to Supernova*, ed. K. van der Hucht, A. Herrero, & C. Esteban (San Francisco, CA: Astronomical Society of the Pacific), 365
- Orosz, J. A., McClintock, J. E., Aufdenberg, J. P., et al. 2011a, *ApJ*, **742**, 84
- Orosz, J. A., Steiner, J. F., McClintock, J. E., et al. 2011b, *ApJ*, **730**, 75
- Panessa, F., Barcons, X., Bassani, L., et al. 2007, *A&A*, **467**, 519
- Park, S. Q., Miller, J. M., McClintock, J. E., et al. 2004, *ApJ*, **610**, 378
- Pastorini, G., Marconi, A., Capetti, A., et al. 2007, *A&A*, **469**, 405
- Perley, R. A., & Butler, B. J. 2013, *ApJS*, **204**, 19
- Peterson, B. M. 2014, *SSRv*, **183**, 253
- Plotkin, R. M., Gallo, E., & Jonker, P. G. 2013, *ApJ*, **773**, 59
- Plotkin, R. M., Markoff, S., Kelly, B. C., Körding, E., & Anderson, S. F. 2012, *MNRAS*, **419**, 267
- Pooley, G. G., & Waldram, E. M. 2000, *IAUC*, **7390**, 2
- Predehl, P., Andritschke, R., Böhringer, H., et al. 2010, *Proc. SPIE*, **7732**, 77320U
- Qian, L., Dong, X.-B., Xie, F.-G., Liu, W., & Li, D. 2017, arXiv:1707.04029
- Reid, M. J., McClintock, J. E., Narayan, R., et al. 2011, *ApJ*, **742**, 83
- Reines, A. E., Sivakoff, G. R., Johnson, K. E., & Brogan, C. L. 2011, *Natur*, **470**, 66
- Richards, J. L., Max-Moerbeck, W., Pavlidou, V., et al. 2011, *ApJS*, **194**, 29
- Rosatì, P., Tozzi, P., Giacconi, R., et al. 2002, *ApJ*, **566**, 667
- Rusli, S. P., Thomas, J., Erwin, P., et al. 2011, *MNRAS*, **410**, 1223
- Rusli, S. P., Thomas, J., Saglia, R. P., et al. 2013, *AJ*, **146**, 45
- Saikia, D. J., Pedlar, A., Unger, S. W., & Axon, D. J. 1994, *MNRAS*, **270**, 46
- Sarzi, M., Rix, H.-W., Shields, J. C., et al. 2001, *ApJ*, **550**, 65

- Sarzi, M., Rix, H.-W., Shields, J. C., et al. 2002, *ApJ*, 567, 237
- Schmitt, H. R., Ulvestad, J. S., Antonucci, R. R. J., & Kinney, A. L. 2001, *ApJS*, 132, 199
- Schulze, A., & Gebhardt, K. 2011, *ApJ*, 729, 21
- Shaposhnikov, N., Swank, J., Shrader, C. R., et al. 2007, *ApJ*, 655, 434
- Shen, J., & Gebhardt, K. 2010, *ApJ*, 711, 484
- Shen, Y., & Ho, L. C. 2014, *Natur*, 513, 210
- Shurkin, K., Dunn, R. J. H., Gentile, G., Taylor, G. B., & Allen, S. W. 2008, *MNRAS*, 383, 923
- Sramek, R. 1975, *AJ*, 80, 771
- Steehgs, D., McClintock, J. E., Parsons, S. G., et al. 2013, *ApJ*, 768, 185
- Strader, J., Chomiuk, L., Maccarone, T. J., Miller-Jones, J. C. A., & Seth, A. C. 2012, *Natur*, 490, 71
- Sulentic, J. W., Zwitter, T., Marziani, P., & Dultzin-Hacyan, D. 2000, *ApJL*, 536, L5
- Tadhunter, C., Marconi, A., Axon, D., et al. 2003, *MNRAS*, 342, 861
- Tananbaum, H., Gursky, H., Kellogg, E., Giacconi, R., & Jones, C. 1972, *ApJL*, 177, L5
- Terrazas, B. A., Bell, E. F., Henriques, B. M. B., et al. 2016, *ApJL*, 830, L12
- Tingay, S. J., Jauncey, D. L., King, E. A., et al. 2003, *PASJ*, 55, 351
- Tonry, J. L., Dressler, A., Blakeslee, J. P., et al. 2001, *ApJ*, 546, 681
- Ulvestad, J. S., & Wilson, A. S. 1984, *ApJ*, 285, 439
- Valluri, M., Ferrarese, L., Merritt, D., & Joseph, C. L. 2005, *ApJ*, 628, 137
- van den Bosch, R. C. E. 2016, *ApJ*, 831, 134
- van den Bosch, R. C. E., & de Zeeuw, P. T. 2010, *MNRAS*, 401, 1770
- van den Bosch, R. C. E., Gebhardt, K., Gültekin, K., et al. 2012, *Natur*, 491, 729
- van der Marel, R. P., & van den Bosch, F. C. 1998, *AJ*, 116, 2220
- Venturi, T., Dallacasa, D., & Stefanachi, F. 2004, *A&A*, 422, 515
- Véron-Cetty, M.-P., & Véron, P. 2006, *A&A*, 455, 773
- Véron-Cetty, M.-P., & Véron, P. 2010, *A&A*, 518, A10
- Walsh, J. L., Barth, A. J., Ho, L. C., & Sarzi, M. 2013, *ApJ*, 770, 86
- Walsh, J. L., Barth, A. J., & Sarzi, M. 2010, *ApJ*, 721, 762
- Walsh, J. L., van den Bosch, R. C. E., Barth, A. J., & Sarzi, M. 2012, *ApJ*, 753, 79
- Wang, R., Wu, X.-B., & Kong, M.-Z. 2006, *ApJ*, 645, 890
- White, R. L., Becker, R. H., Helfand, D. J., & Gregg, M. D. 1997, *ApJ*, 475, 479
- Wold, M., Lacy, M., Käufel, H. U., & Siebenmorgen, R. 2006, *A&A*, 460, 449
- Wright, A., & Otrupcek, R. 1990, PKS Catalog
- Wrobel, J. M., & Heeschen, D. S. 1984, *ApJ*, 287, 41
- Wrobel, J. M., & Heeschen, D. S. 1991, *AJ*, 101, 148
- Xanthopoulos, E., Thean, A. H. C., Pedlar, A., & Richards, A. M. S. 2010, *MNRAS*, 404, 1966
- Xie, F.-G., & Yuan, F. 2016, *MNRAS*, 456, 4377
- Xie, F.-G., & Yuan, F. 2017, *ApJ*, 836, 104
- Yamauchi, A., Nakai, N., Ishihara, Y., Diamond, P., & Sato, N. 2012, *PASJ*, 64, 103
- Yang, Y., Li, Z., Sjouwerman, L. O., et al. 2015, *ApJL*, 807, L19
- Yuan, F., & Cui, W. 2005, *ApJ*, 629, 408
- Zhao, J.-H., Bower, G. C., & Goss, W. M. 2001, *ApJL*, 547, L29